Avalanche effects in phase transition modulated thermal convection: A model of Earth's mantle

L. P. Solheim and W. R. Peltier

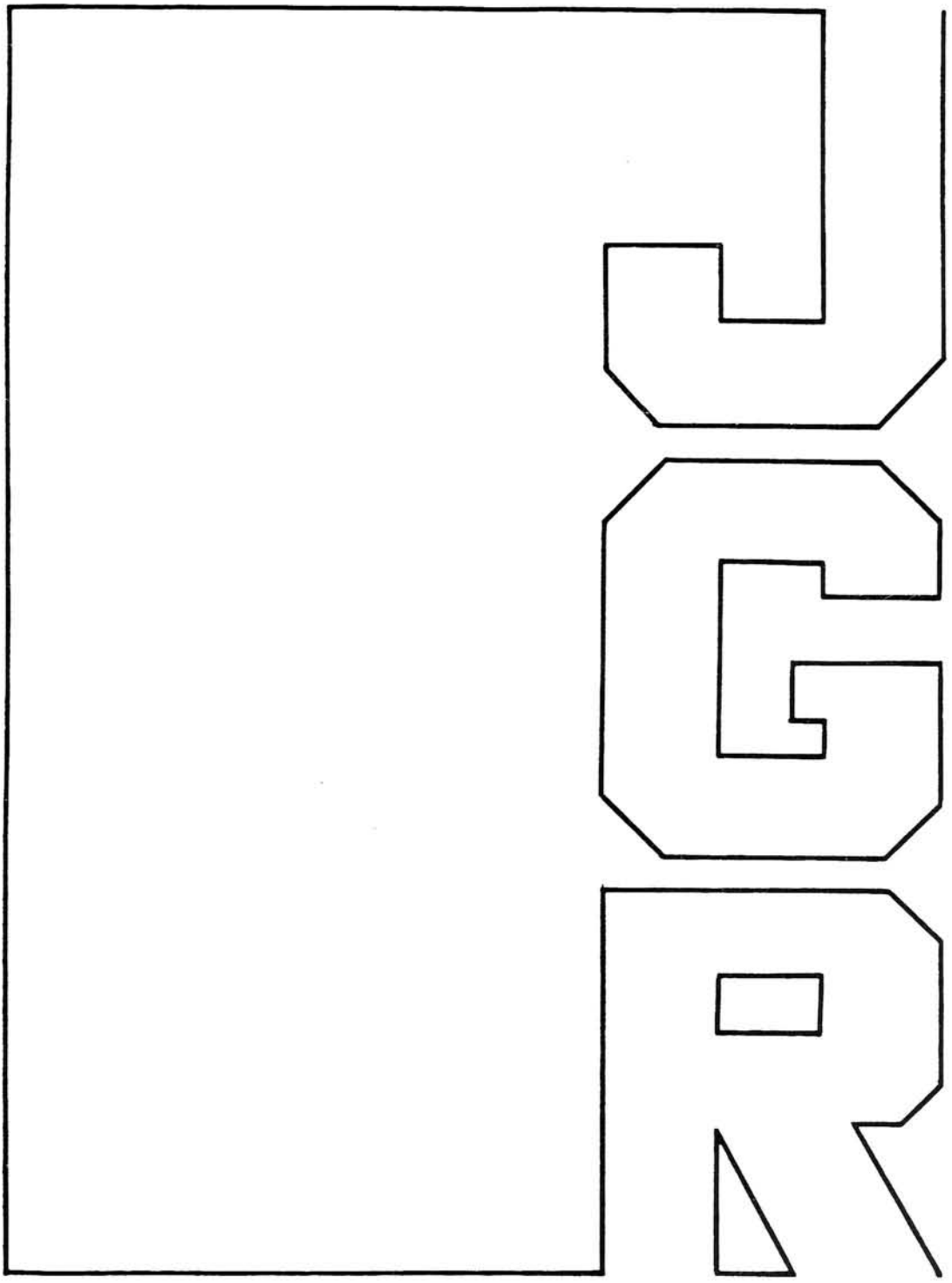

JOURNAL OF GEOPHYSICAL RESEARCH, VOL. 99, NO. B4, APRIL 10, 1994

JOURNAL OF GEOPHYSICAL RESEARCH, VOL. 99, NO. B4, PAGES 6997–7018, APRIL 10, 1994

Avalanche effects in phase transition modulated thermal convection: A model of Earth's mantle

L. P. Solheim and W. R. Peltier

Department of Physics, University of Toronto, Toronto, Ontario, Canada

Abstract. We describe the development and application of an anelastic, multiphase model of the mantle convection process in axisymmetric spherical shell geometry. The radial structure of the anelastic reference state has been determined on the basis of elastic wave propagation data, primarily those used to construct the preliminary reference Earth model (PREM). The multiphase model is employed to examine the extent to which the pressure-induced phase transitions in the planetary mantle may conspire to cause the flow to become radially layered. We find that the endothermic phase transition at 670 km depth profoundly influences the radial mixing process in the high Rayleigh number regime. In the Earth-like region of parameter space the flow exhibits a low-frequency quasi-periodicity characterized by rather long periods of relative quiescence in which the circulation is predominantly layered followed by short periods of intense radial mixing across the endothermic horizon. These "avalanche" events are controlled by the periodic instability of the internal thermal boundary layer that develops on the endothermic horizon when the flow is layered. This hydrodynamic process appears to have important implications for the understanding of a number of characteristics of planetary evolution, especially thermal and chemical history.

Introduction

Many different spherical shell models of the thermal convection process have been presented in the recent literature that have been employed to study various aspects of mantle mixing [*Hsui et al.*, 1972; *Young*, 1974; *Weir*, 1976, 1978; *Schubert and Zebib*, 1980; *Zebib et al.*, 1980, 1983; *Baumgardner*, 1985; *Zebib et al.*, 1985; *Machetel and Rabinowicz*, 1986; *Glatzmaier*, 1988; *Machetel and Yuen*, 1989; *Bercovici et al.*, 1989; *Solheim and Peltier*, 1990; *Glatzmaier et al.*, 1990; *Machetel and Weber*, 1991]. Because the viscous fluid dynamics of this region of the planetary interior, roughly the outer 50% by radius, is intimately involved in the process of continental drift, it is not surprising that the subject continues to inspire such a high level of research activity. Despite this activity, there remain a number of key issues which still need to be satisfactorily addressed. These issues include the fundamental question of the role of phase transitions in the mantle general circulation, especially concerning the degree of radial layering that may result from their presence. Our purpose in this paper is to describe an axisymmetric, anelastic model of the thermal convection process with which it has been possible to simulate the influence on the circulation of either or both of the major solid-solid phase transformations that exist at 400 km and 670 km depth in the planetary mantle. The time independent, spherically averaged anelastic reference state is derived on the basis of best current estimates of the radial dependence of the appropriate thermodynamic parameters, primarily from the preliminary reference earth model (PREM) of *Dziewonski and Anderson* [1981]. Previous versions of our model have been employed to study various aspects of the mantle convection process; in particular, the nature of the chaotic mixing that characterizes the dynamical state in the regime of high Rayleigh number [*Solheim and Peltier*, 1990].

The major seismic discontinuities that exist in the Earth occur at depths of 400 km and 670 km. These discontinuities have been shown to be a consequence of solid-solid pressure-induced phase transformations of the mantle mineralogy. The 400-km boundary is known to be due primarily to a transformation of the olivine constituent, $(Mg_{(1-x)}Fe_x)_2SiO_4$, which is the dominant material of the upper mantle with $x \approx 0.1$, to the spinel phase. This high-pressure phase of olivine was first reported by *Ringwood and Major* [1966, 1970] and *Akimoto and Fujisawa* [1966]. *Liu* [1975] first showed that the spinel structure transforms further at higher pressure to a mixture of magnesiowüstite, (Mg,Fe)O, and perovskite $(Mg,Fe)SiO_3$ at temperatures and pressures that obtain near 670 km depth in the mantle via the reaction:

$$(Mg,Fe)_2SiO_4 \rightarrow (Mg,Fe)O + (Mg, Fe)SiO_3.$$

The 400-km transformation is exothermic, having a positive Clapeyron slope β_1 between +2.0 MPa/K and +3.0 MPa/K [*Akimoto et al.*, 1976; *Jeanloz and Thompson*, 1983; *Weidner et al.*, 1984; *Weidner*, 1985; *Akaogi et al.*, 1989; *Katsura and Ito*, 1989] and takes place over a depth range of 18 ± 5 km [*Akaogi et al.*, 1989], while the 670-km phase change is endothermic, having a negative Clapeyron slope β_2 between −2 MPa/K and −3 MPa/K [*Liu*, 1976; *Ito*, 1977; *Jeanloz and Thompson*, 1983; *Ito and Takahashi*, 1989] and occurs over a much narrower depth range ≤4 km [*Ito and Takahashi*, 1989]. More recent results indicate that the value of the 670 km Clapeyron slope may actually be as negative as −4.0 ± 2.0 MPa/K [*Ito et al.*, 1990].

There are, in fact, a number of transformations of upper mantle minerals that occur above 670 km depth. Along the geotherm (the depth dependent azimuthaly averaged temper-

Paper number 93JB02168.
0148-0227/94/93JB-02168$05.00

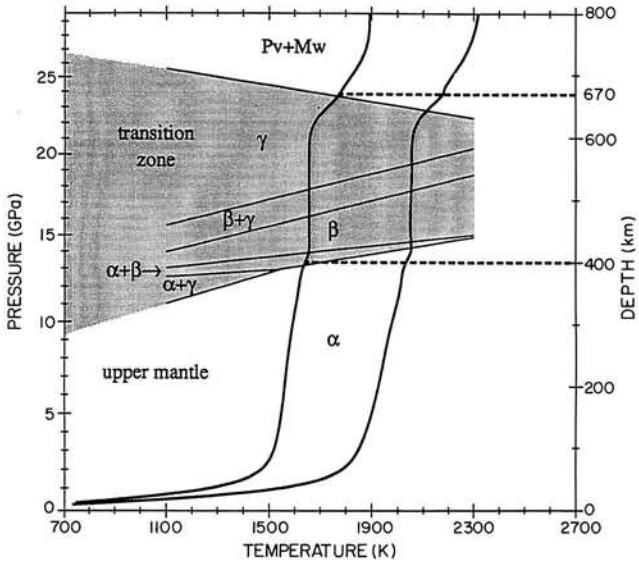

Figure 1. Phase boundaries for the $\alpha \rightarrow \beta \rightarrow \gamma$ transitions of $(Mg_{0.89}Fe_{0.11})_2SiO_4$ (thin solid lines) are overlain on two model geotherms (heavy solid lines). The phase boundaries are from *Akaogi et al.* [1989] and the geotherms are from two simulations performed with the multiphase model of chapter 3, with $Ra = 10^7$, $\beta_1 = +3.0$ MPa/K and $\beta_2 = -2.8$ MPa/K. In one simulation there was no internal heating (left curve) and in the other (right curve), internal heating corresponding to $\mu = 10$ was used. The geotherm in the real Earth likely falls somewhere in between the two curves shown.

ature), olivine (α) transforms first to modified spinel (β) through a mixed phase region consisting of $\alpha + \beta$, then to spinel (γ) through a mixed phase region of $\beta + \gamma$, in the transition zone of the mantle. There is, however, a region in P-T space for $\alpha + \gamma$ through which cold sinking thermal plumes may pass. The phase boundaries for these transformations have been computed for $(Mg_{0.89}Fe_{0.11})_2SiO_4$ by *Akaogi et al.* [1989] and are shown in Figure 1 along with two model geotherms from the hydrodynamic simulations to be discussed below. $(Mg_{0.89}Fe_{0.11})_2SiO_4$ is representative of mantle olivine [*Ringwood*, 1975]. The light solid lines of Figure 1 represent the phase boundaries, and the areas between these lines are labeled with the appropriate phases. The two heavy solid lines illustrate two temporally averaged geotherms from our simulations in which the Rayleigh number $Ra = 10^7$, $\beta_1 = +3.0$ MPa/K and $\beta_2 = -2.8$ MPa/K. The two simulations that result in these geotherms differ in that one corresponds to a case in which the fluid is heated entirely from below (the low-temperature curve) and one has internal heating corresponding to $\mu = 10$ (the high-temperature curve), where μ is a parameter to be defined in what follows that measures the fraction of the net heating that drives the convective circulation that is derivative of internal sources as opposed to that applied through the lower boundary. With $\mu = 10$, as will be discussed in more detail below, roughly 50% of the heating is from below and 50% is from within. The geotherm in Earth's mantle likely lies in the region between these two curves. Although the 400-km and 670-km seismic discontinuities are by far the strongest reflectors of seismic energy, other discontinuities exist through the so-called transition zone that is bracketed by these horizons. In particular, *Shearer* [1990] has found evidence for the existence of discontinuities at 410 km, 520 km, and 660 km using stacked images of long-period seismic data. The existence of a seismic reflector at 520 km can be explained by the presence of the $\beta \rightarrow \beta + \gamma \rightarrow \gamma$ transition that appears at that depth (see Figure 1). In fact, it would be difficult to accept Figure 1 as a correct representation of the mantle phase diagram if this discontinuity did not appear in the seismic data. The fact that Shearer determines the boundaries of the transition zone to be at 410 km and 660 km rather than at 400 km and 670 km, the levels to which they correspond in PREM, provides some indication as to the uncertainty of these average depths. The coincidence of three seismic reflectors at the calculated positions of the three transformations of olivine through the transition zone suggests that Figure 1 provides a rather accurate representation of the mantle above 670 km depth and that the geotherm does lie in the intermediate region between the two geotherms shown in Figure 1.

It was knowledge of these phase equilibria that first sparked speculation as to whether the mantle may be convecting in two layers, one above 670 km and one below 670 km. Various geophysical observations [*Peltier and Jarvis*, 1982] have been employed to argue in favor of either the layered scenario or the "whole mantle" scenario. Proponents of the layered model have usually argued that the 670-km seismic discontinuity was a consequence of a chemical difference between the upper and lower mantle as well as corresponding to the spinel → post-spinel phase change. The primary reason for this was that the seismically observed thickness of this boundary is only a few kilometers, and it was thought that this was much too narrow to be caused entirely by an equilibrium phase change. It has recently been demonstrated, however, that the phase loop thickness for the 670-km phase change is in fact only a few kilometers [*Ito and Takahashi*, 1989], as mentioned above. There appears to be no good reason to believe therefore that the 670-km seismic horizon is associated with any effect other than that due to the spinel to magnesiowüstite and perovskite phase transformation. Even though the 670-km boundary may have no change of mean atomic weight across it, it is nevertheless possible that an endothermic phase change may strongly inhibit the advection of material across it. This is, in fact, very likely to be the state of the present-day earth as we shall demonstrate in what follows. Previous preliminary analyses of this issue have been presented by *Machetel and Weber* [1991] for the axisymmetric spherical shell whose results were obtained for a Rayleigh number of approximately 10^6, well below that for the modern Earth (10^7) and by *Peltier and Solheim* [1992] in the same geometry for a Rayleigh number of 10^7. The former analysis revealed only weak layering with a Clapeyron slope for the endothermic transition of -3 MPa/K, whereas the latter obtained quite strong layering with the Clapeyron slope near this same value. The recently published results on the impact of the endothermic transition in three-dimensional spherical geometry by *Tackley et al.* [1993] were obtained for thermal forcing very close to that employed by Machetel and Weber and the degree of layering revealed by the analysis is much less pronounced than that obtained by Peltier and Solheim at the higher Rayleigh number, suggesting that the effect of the geometrical difference may be modest. The issue of the degree of layering characteristic of the modern earth is important and therefore warrants detailed analysis in the context of the axisymmetric spherical shell. Our arguments are based upon detailed numerical simulations with a new multiphase con-

vection model, and the results are employed to determine the influence on layering of the main control variables of the model which include the Rayleigh number Ra, the internal heating parameter μ, as well as the phase loop thicknesses and the Clapeyron slopes of both the 400-km and 670-km phase transformations. We document the specific circumstances under which layering arises and describe the time dependence of some of these highly nonlinear flows. This time dependence is of some interest because it displays a quasi-periodicity in which certain "avalanche" events repeat themselves every 600–800 m.y. in our axisymmetric model. We begin with a complete description of the multiphase model and continue with a detailed analysis of the influence of individual parameters on the simulated flows.

Multiphase, Anelastic Convection Model

The system of equations we shall employ to represent the thermal convection process in a multiphase mantle is based on the usual field equations describing the pointwise conservation of mass, momentum, and internal energy for a Newtonian fluid (equations (1)–(3)), completed with an appropriate equation of state (4):

$$\frac{\partial \rho}{\partial t} + \nabla \cdot (\rho \mathbf{u}) = 0 \tag{1}$$

$$\rho \frac{D\mathbf{u}}{Dt} = \rho g - \nabla p - \nabla \times (\eta \nabla \times \mathbf{u}) + \tfrac{4}{3} \nabla (\eta \nabla \cdot \mathbf{u}) \tag{2}$$

$$\rho c_p \frac{DT}{Dt} - \alpha T \frac{Dp}{Dt} = \nabla \cdot k \nabla T + \rho \chi + \Phi + \rho \frac{D}{Dt} (l_1 \Gamma_1 + l_2 \Gamma_2) \tag{3}$$

$$\rho = \rho_r \left\{ 1 - \alpha (T - T_r) + \frac{1}{K_T} (p - p_r) \right\} + \Delta_1 (\Gamma_1 - \Gamma_{r_1}) + \Delta_2 (\Gamma_2 - \Gamma_{r_2}). \tag{4}$$

In this system of equations, ρ, $\mathbf{u}$, p, and T are density, velocity, pressure, and temperature, respectively, while g, η, c_p, α, k, and K_T are gravitational acceleration, molecular viscosity, specific heat capacity at constant pressure, thermal expansion coefficient, thermal conductivity, and isothermal bulk modulus, respectively; χ is a constant heating rate per unit mass, and Φ represents the viscous dissipation rate per unit volume of fluid. For spherical axisymmetric geometry the dissipation function Φ has the explicit form

$$\Phi = \eta \left\{ 2 \left[\frac{\partial u_r}{\partial r} \right]^2 + 2 \left[\frac{1}{r} \frac{\partial u_\theta}{\partial \theta} + \frac{u_r}{r} \right]^2 + 2 \left[\frac{u_r}{r} + \frac{u_\theta \cot \theta}{r} \right]^2 + \left[\frac{\partial u_\theta}{\partial r} - \frac{u_\theta}{r} + \frac{1}{r} \frac{\partial u_r}{\partial \theta} \right]^2 - \tfrac{1}{3} [\nabla \cdot \mathbf{u}]^2 \right\}. \tag{5}$$

The last term on the right-hand side of (3) accounts for the release (absorption) of latent heat during a change of phase. The terms l_1 and l_2 are the energy per unit mass released (or absorbed) as the fluid changes from phase 1 to phase 2 (olivine-spinel) or from phase 2 to phase 3 (spinel-perovskite and magnesiowüstite), respectively. The phase density functions $\Gamma_1(r, \theta, t)$ and $\Gamma_2(r, \theta, t)$ are the fractions of phase 2 or phase 3, respectively, that exist at any position in the mantle at any time and are specifically represented as

$$\Gamma_i = \frac{1}{2} \left\{ 1 + \tanh \left[(r_{p_i}(\theta, t) - r) \frac{h_i}{d} \right] \right\}. \tag{6}$$

The form of Γ_i (equation (6)) is chosen following *Richter* [1973] and allows for a finite depth (determined by the parameter h_i) over which the phase change takes place; $r_{p_i}(\theta, t)$ is the radial position of the ith phase boundary at azimuthal location (θ) and time (t), while d is the depth of the convecting region, here the mantle thickness. Note that when $r = r_{p_i}$, $\Gamma_i = 1/2$. Thus the location of a given phase boundary is defined to be that point at which 50% of each phase is present.

The equation of state (4) is simply a linear Taylor expansion of the density about a background state with the last two terms on the right-hand side added to incorporate the density variation due to the phase changes. The spherically averaged reference state has density $\rho_r(r)$, temperature $T_r(r)$, and pressure $p_r(r)$ and is characterized by the phase density functions $\Gamma_{r_1}(r)$ and $\Gamma_{r_2}(r)$. $\Delta_1 = \rho_2 - \rho_1$ and $\Delta_2 = \rho_3 - \rho_2$ are the differences in densities between phase 2 and phase 1 across phase boundary 1 and between phase 3 and phase 2 across phase boundary 2, respectively.

The anelastic-liquid approximation [e.g., *Jarvis and McKenzie*, 1980] is applied to the system (1)–(4). This involves setting $\partial \rho / \partial t = 0$ in 1, assuming g, c_p, α, k, K_T, and κ (thermal diffusivity) to be known functions of radius and replacing ρ by ρ_r everywhere in (1)–(3) except in the body force term of (2). Because the mantle has essentially infinite Prandtl number, the inertial force term in the momentum conservation equation may be neglected [*Peltier*, 1972]. Furthermore, owing to the extremely small velocities associated with the mantle convection process, the pressure distribution is very nearly that of a fluid in hydrostatic equilibrium and we may then safely assume

$$\alpha T \frac{Dp}{Dt} \simeq -\alpha T \rho g u_r. \tag{7}$$

These approximations have been discussed in greater detail by *Solheim and Peltier* [1990].

We nondimensionalize the system (1)–(4) according to relations (8), in which the subscript zero identifies a reference value, $d = 2.89 \times 10^6$ m is the depth scale (mantle thickness), and $T_c = T_{\text{cmb}} - T_{\text{sur}}$ is the temperature scale.

$$r = dr', \quad t = \frac{\eta_0}{\rho_0 \alpha_0 T_c g_0 d} t', \quad \mathbf{u} = \frac{\rho_0 \alpha_0 T_c g_0 d^2}{\eta_0} \mathbf{u}',$$

$$T = T_c T' + T_0, \quad p = \rho_0 g_0 d p', \quad \rho = \rho_0 \rho',$$

$$\alpha = \alpha_0 \alpha', \quad \kappa = \frac{k_0}{\rho_0 c_{p_0}} \kappa', \quad k = k_0 k', \tag{8}$$

$$K_T = \rho_0 g_0 d K_T', \quad g = g_0 g', \quad c_p = c_{p_0} c_p',$$

$$l_i = g_0 d l_i', \quad Ra = \frac{\alpha_0 T_c g_0 d^3 \rho_0^2 c_{p_0}}{k_0 \eta_0}.$$

Equations (8), together with the approximations discussed above, transform (1)–(4) into the nondimensional system

(9)–(12). After dropping the primes denoting nondimensional values we obtain:

$$\nabla \cdot (\rho_r \mathbf{u}) = 0 \tag{9}$$

$$0 = -\rho g \hat{\mathbf{r}} - \nabla p + \alpha_0 T_c \{\nabla \times (\nabla \times \mathbf{u}) + \tfrac{4}{3} \nabla \cdot \mathbf{u}\} \tag{10}$$

$$\frac{DT}{Dt} - \frac{\tau_0}{\alpha_0 T_c c_p} \frac{D}{Dt} (l_1\Gamma_1 + l_2\Gamma_2) = \frac{\kappa}{Ra} \left[\nabla^2 T + \frac{1}{k} \frac{\partial k}{\partial r} \frac{\partial T}{\partial r}\right] + \frac{\mu}{c_p Ra} + \frac{\tau_0 \Phi}{\rho_r c_p} - \tau u_r (T + T_0) \tag{11}$$

$$\rho = \rho_r \left\{1 - \alpha_0 T_c \alpha (T - T_r) + \frac{1}{K_T} (p - p_r)\right\} + \Delta_1(\Gamma_1 - \Gamma_{r_1}) + \Delta_2(\Gamma_2 - \Gamma_{r_2}). \tag{12}$$

This introduces three additional nondimensional groups besides the Rayleigh number Ra; the internal heating parameter μ, the dissipation function [*Peltier*, 1972] $\tau(r)$, and the reference value for the dissipation function τ_0,

$$\mu = \frac{\rho_0 \chi d^2}{k_0 T_c} \qquad \tau_0 = \frac{g_0 \alpha_0 d}{c_{p_0}} \qquad \tau(r) = \tau_0 \frac{g\alpha}{c_p}. \tag{13}$$

Numerical Formulation of the Model Equations

In axisymmetric spherical geometry the velocity field, $\mathbf{u} = (u_r, u_\theta, 0)$, may be written in terms of a streamfunction ψ such that (9) is satisfied identically, namely,

$$u_r = \frac{1}{\rho_r r^2 \sin\theta} \frac{\partial \psi}{\partial \theta}, \qquad u_\theta = \frac{-1}{\rho_r r \sin\theta} \frac{\partial \psi}{\partial r}. \tag{14}$$

From the definition of the vorticity field $\omega = \nabla \times \mathbf{u} = (0, 0, \omega)$ we then have

$$\frac{\partial^2 \psi}{\partial r^2} - \frac{1}{\rho_r} \frac{\partial \rho_r}{\partial r} \frac{\partial \psi}{\partial r} + \frac{1}{r^2} \frac{\partial^2 \psi}{\partial \theta^2} - \frac{\cot\theta}{r^2} \frac{\partial \psi}{\partial \theta} = -\rho_r r \omega \sin\theta. \tag{15}$$

Operating on (10) with $\nabla\times$ and transforming the vorticity to $w = \omega r \sin\theta$ delivers the following partial differential equation for w:

$$\frac{\partial^2 w}{\partial r^2} + \frac{1}{r^2} \frac{\partial^2 w}{\partial \theta^2} - \frac{\cot\theta}{r^2} \frac{\partial w}{\partial \theta} = -\frac{g \sin\theta}{\alpha_0 T_c} \frac{\partial \rho}{\partial \theta}. \tag{16}$$

This vorticity transformation renders identical the operators that must be inverted to obtain ψ and w, thus reducing memory and cpu time requirements in the numerical solution. With the aid of (12) we may rewrite (16) as

$$\frac{\partial^2 w}{\partial r^2} + \frac{g\rho_r}{K_T} \frac{\partial w}{\partial r} + \frac{1}{r^2} \frac{\partial^2 w}{\partial \theta^2} - \frac{\cot\theta}{r^2} \frac{\partial w}{\partial \theta} = g \sin\theta \left(\rho_r \alpha \frac{\partial T}{\partial \theta} - \frac{\Delta_1}{\alpha_0 T_c} \frac{\partial \Gamma_1}{\partial \theta} - \frac{\Delta_2}{\alpha_0 T_c} \frac{\partial \Gamma_2}{\partial \theta} + \frac{4}{3K_T} \frac{\partial \rho_r}{\partial r} \frac{\partial u_r}{\partial \theta}\right).$$

Inspection of (11) reveals that there are two distinct terms that involve total time derivatives. Defining a new "temperature" as

$$A = T - \frac{\tau_0}{\alpha_0 T_c c_p} (l_1\Gamma_1 + l_2\Gamma_2) \tag{17}$$

reduces to one the number of terms in the energy equation that involve an explicit time derivative. Because this transformation eliminates explicit time derivatives on three functions (derivatives of T and $\Gamma_{1,2}$) in favor of an explicit time derivative on only one function (the "transformed temperature" A), it eliminates the numerical problems that would otherwise be associated with the advection of three separate quantities. Eliminating T in favor of A, we may rewrite the system (17), (15), and (11) (after some algebraic manipulation) into the form

$$\frac{\partial^2 w}{\partial r^2} + \frac{g\rho_r}{K_T} \frac{\partial w}{\partial r} + \frac{1}{r^2} \frac{\partial^2 w}{\partial \theta^2} - \frac{\cot\theta}{r^2} \frac{\partial w}{\partial \theta} = \frac{4g}{3K_T \rho_r} \frac{\partial \rho_r}{\partial r} \cdot \left\{\frac{1}{r^2} \frac{\partial^2 \psi}{\partial \theta^2} - \frac{\cot\theta}{r^2} \frac{\partial \psi}{\partial \theta}\right\} + \rho_r \alpha g \sin\theta \cdot \left\{\frac{\partial A}{\partial \theta} + \frac{2h_1\Gamma_1(1-\Gamma_1)}{\alpha_0 T_c} \left(\frac{\tau_0 l_1}{c_p} - \frac{\Delta_1}{\rho_r \alpha}\right) \frac{\partial r_{p_1}}{\partial \theta} + \frac{2h_2\Gamma_2(1-\Gamma_2)}{\alpha_0 T_c} \left(\frac{\tau_0 l_2}{c_p} - \frac{\Delta_2}{\rho_r \alpha}\right) \frac{\partial r_{p_2}}{\partial \theta}\right\} \tag{18}$$

$$\frac{\partial^2 \psi}{\partial r^2} - \frac{1}{\rho_r} \frac{\partial \rho_r}{\partial r} \frac{\partial \psi}{\partial r} + \frac{1}{r^2} \frac{\partial^2 \psi}{\partial \theta^2} - \frac{\cot\theta}{r^2} \frac{\partial \psi}{\partial \theta} = -w\rho_r \tag{19}$$

$$\frac{\partial A}{\partial t} = \frac{\kappa}{Ra} D^2 A - \frac{J(A, \psi)}{\rho_r r^2 \sin\theta} + \frac{\mu}{c_p Ra} + \frac{\tau_0 \Phi}{\rho_r c_p} - \frac{\tau(A + T_0)}{\rho_r r^2 \sin\theta} \frac{\partial \psi}{\partial \theta} + \zeta \tag{20}$$

in which $J(\ ,\ ) \equiv \partial(\ ,\ )/\partial(r, \theta)$ is the Jacobian operator, D^2 is the operator

$$D^2 \equiv \frac{\partial^2}{\partial r^2} + \left(\frac{2}{r} + \frac{1}{k} \frac{\partial k}{\partial r}\right) \frac{\partial}{\partial r} + \frac{1}{r^2} \frac{\partial^2}{\partial \theta^2} + \frac{\cot\theta}{r^2} \frac{\partial}{\partial \theta},$$

and

$$\zeta = \frac{\tau_0}{\alpha_0 T_c c_p} \left\{(l_1\Gamma_1 + l_2\Gamma_2)\left[\left(\frac{1}{c_p} \frac{\partial c_p}{\partial r} - \tau\right) u_r - \frac{\kappa}{Ra} \left(\frac{1}{c_p} \frac{\partial^2 c_p}{\partial r^2} - \left(\frac{2}{r} + \frac{1}{k} \frac{\partial k}{\partial r} - \frac{2}{c_p} \frac{\partial c_p}{\partial r}\right) \frac{1}{c_p} \frac{\partial c_p}{\partial r}\right)\right] + 2l_1h_1\Gamma_1(1-\Gamma_1) \frac{\kappa}{Ra} \left[\frac{1}{r^2} \left(\frac{\partial^2 r_{p_1}}{\partial \theta^2} + \cot\theta \frac{\partial r_{p_1}}{\partial \theta}\right) - \left(\frac{2}{r} + \frac{1}{k} \frac{\partial k}{\partial r} - \frac{2}{c_p} \frac{\partial c_p}{\partial r}\right) + 2h_1(1 - 2\Gamma_1)\right.$$

$$\cdot\left(1+\frac{1}{r^2}\left(\frac{\partial r_{p_1}}{\partial\theta}\right)^2\right)\Bigg] + 2l_2h_2\Gamma_2(1-\Gamma_2)\,\frac{\kappa}{Ra}$$

$$\cdot\left[\frac{1}{r^2}\left(\frac{\partial^2 r_{p_2}}{\partial\theta^2}+\cot\theta\,\frac{\partial r_{p_2}}{\partial\theta}\right)-\left(\frac{2}{r}+\frac{1}{k}\frac{\partial k}{\partial r}-\frac{2}{c_p}\frac{\partial c_p}{\partial r}\right)\right.$$

$$\left.+\,2h_2(1-2\Gamma_2)\left(1+\frac{1}{r^2}\left(\frac{\partial r_{p^2}}{\partial\theta}\right)^2\right)\right]\Bigg\}.$$

By incorporating phase boundaries into the model, we have introduced two additional unknowns, $r_{p_1}(\theta, t)$ and $r_{p_2}(\theta, t)$, which together with w, ψ, and A constitute a total of five dependent variables. We therefore require two further equations (besides (18)–(20)) to complete the system. These arise from the fact that the position of a phase boundary is determined by its Clapeyron slope. If we assume a linear p-T relationship across a phase boundary (i.e., a constant Clapeyron slope for each transition), then $p = p_0 + \beta T$, where p_0 is the zero temperature pressure and $\beta = dp/dT$ is the Clapeyron slope. We can write this in dimensionless form, for the ith phase boundary, as

$$p = p_{0_i} + \beta_i(T + T_0) \qquad i = 1, 2. \tag{21}$$

Here, T_0 is the nondimensional (scaled by T_c) surface temperature. We may further rewrite (21) in terms of the transformed temperature A (equation (17)) and replace $p(r, \theta, t)$ by $p_r(r)$ (a reasonable approximation for the mantle). Then keeping in mind that (21) is only satisfied at the position of the ith phase boundary and that $\Gamma_i = 1/2$ when $r = r_{p_i}$, we obtain the following equations which are valid at the position of phase boundary 1 and phase boundary 2, respectively:

$$\beta_1\left\{A + T_0 + \frac{\tau_0}{2\alpha_0 T_c c_p}\left[l_1 + l_2 + l_2\tanh\left((r_{p_2} - r_{p_1})h_2\right)\right]\right\} + p_0 - p_r = 0, \tag{22}$$

$$\beta_2\left\{A + T_0 + \frac{\tau_0}{2\alpha_0 T_c c_p}\left[l_1 + l_2 + l_1\tanh\left((r_{p_1} - r_{p_2})h_1\right)\right]\right\} + p_0 - p_r = 0. \tag{23}$$

At a particular azimuthal location θ and time t, r_{p_1} and r_{p_2} will be the zeros of the coupled system (22) and (23). If only phase boundary 1 is present, then we may set $l_2 = 0$ and r_{p_1} is the zero of (22). Similarly if only phase boundary 2 is present, then we set $l_1 = 0$ and r_{p_2} is the zero of (23).

It will be noted that β_i and l_i are not independent parameters but rather are related through the (nondimensional) Clapeyron equation

$$\beta_i = \frac{\rho^2 l_i}{(T + T_0)\Delta_i} \tag{24}$$

in which ρ and T are the density and temperature at the position of the ith phase boundary. In practice, only β_i was specified as a parameter of the model, and the l_i were calculated using (24) and the average density and temperature at the depth of the ith phase boundary.

The system (18)–(20), (22), and (23) was solved numerically on Cray XMP/2-8 and Cray YMP/4-64 supercomputers using a multigrid algorithm written by J. Adams at NCAR to invert the elliptic operators in (18) and (19), while a modified Crank-Nicolson scheme (similar to that discussed by *Solheim and Peltier* [1990]) was used to advance $A(r, \theta, t)$ in time using (20). The zeros of (22) and (23) were determined using the Levenberg-Marquardt algorithm [*Moré et al.*, 1980] for the coupled system or *Müller*'s [1956] method in either of the single-phase boundary cases. With each new $A(r, \theta, t)$, a new right-hand side of (18) can be formed; thus a new w and ψ can be calculated from (18) and (19). This in turn is used to update A, and so the system is stepped through time. The right-hand side of (18) also contains ψ which means that (18) and (19) must be solved iteratively at each time step until a self-consistent stream function and vorticity pair are determined. Note that the effect of either phase boundary may be eliminated simply by setting $l_i = \Delta_i = 0$. Similarly, the latent heat effects or buoyancy effects of either phase change may be eliminated by setting l_i or Δ_i to zero independently. In what follows we will not be able to explore the full range of problems to which this model is applicable but will focus our attention on the impact upon simulated flows of variations in the primary phase transition related variables.

Boundary Conditions

Since there can be no mass flux across any external boundary, the kinematic condition $\psi = 0$ obtains along all four boundaries of the spherical axisymmetric model ($r = r_{\text{cmb}}, r_{\text{sur}}$, and $\theta = 0, \pi$). In order for the vorticity to remain finite along the axes we insist that $w = 0$ on $\theta = 0, \pi$. The condition of zero tangential stress

$$\frac{1}{2}\left\{r\frac{\partial}{\partial r}\left(\frac{u_\theta}{r}\right)+\frac{1}{r}\frac{\partial u_r}{\partial\theta}\right\} = 0$$

together with the relation between w and velocity

$$w = \left\{\frac{\partial r u_\theta}{\partial r} - \frac{\partial u_r}{\partial\theta}\right\}\sin\theta$$

applied along a boundary on which $u_r \equiv 0$ gives the boundary condition on w at a free slip radial boundary, either the core-mantle boundary or the surface, as

$$w = -\frac{2}{r\rho_r}\frac{\partial\psi}{\partial r}. \tag{25}$$

The boundary conditions on A are derived from the conditions on T and r_{p_i}. Owing to the axial symmetry

$$\frac{\partial T}{\partial\theta} = \frac{\partial r_{p_1}}{\partial\theta} = \frac{\partial r_{p_2}}{\partial\theta} = 0$$

along the axes $\theta = 0, \pi$. Therefore

$$\frac{\partial A}{\partial\theta} = \frac{\partial T}{\partial\theta} - \frac{2\tau_0}{\alpha_0 T_c c_p}$$

$$\cdot\left\{l_1h_1\Gamma_1(1-\Gamma_1)\frac{\partial r_{p_1}}{\partial\theta} + l_2h_2\Gamma_2(1-\Gamma_2)\frac{\partial r_{p_2}}{\partial\theta}\right\} = 0 \tag{26}$$

Table 1. Definition of Reference State Curves

f	a_0	a_1	$a2$	a_3	Reference Value
ρ_r					4×10^3 kg m^{-3}
lm	1.975750	−0.708466	0.267906	−0.068475	
tz	2.414630	−0.718113	0	0	
um	1.566632	−0.329520	0	0	
g					10 m s^{-2}
lm	3.067837	−3.411438	1.854549	−0.332736	
tz	1.097924	−0.048916	0	0	
um	1.204020	−0.100267	0	0	
Ks					$\rho_0 g_0 d$
lm	12.217949	−7.449310	2.282883	−0.500992	
tz	14.211461	−6.083397	0	0	
um	7.584351	−2.944444	0	0	
c_p					1250 J kg^{-1} K^{-1}
lm	1.276325	−0.526085	0.326363	−0.0636597	
tz	0.981151	0.011989	0	0	
um	1.125889	−0.056516	0	0	
k					10 W m^{-1} K^{-1}
lm	4.702851	−4.116832	1.065515	−0.051858	
tz	−10.864189	24.899376	−16.390179	3.348804	
um	−10.864189	24.899376	−16.390179	3.348804	
p_r	3.289767	−2.046209	0.227745	0.010324	$\rho_0 g_0 d$

The a_i are nondimensional. $f = a_0 + a_1 r + a_2 r^2 + a_3 r^3$; lm, lower mantle; tz, transition zone; um, upper mantle.

along the axes $\theta = 0, \pi$. At the surface, $T = 0$ and at the cmb, $T = 1$ (nondimensional). We have imposed no constraint on Γ_i as r_{p_i} approaches either radial boundary, so that the boundary conditions on A are

$$A = \frac{-\tau_0}{2\alpha_0 T_c c_p(r_{\text{sur}})} \{l_1 + l_2 + l_1 \tanh [(r_{p_1} - r_{\text{sur}})h_1] + l_2 \tanh [(r_{p_2} - r_{\text{sur}})h_2]\} \quad (27)$$

at the surface and

$$A = 1 - \frac{\tau_0}{2\alpha_0 T_c c_p(r_{\text{cmb}})} \{l_1 + l_2 + l_1 \tanh [(r_{p_1} - r_{\text{cmb}})h_1] + l_2 \tanh [(r_{p_2} - r_{\text{cmb}})h_2]\} \quad (28)$$

at the core-mantle boundary (CMB). Note that these conditions on A may vary in space and time since $r_{p_i} = r_{p_i}(\theta, t)$. If the phase boundaries remain sufficiently far from the surface or CMB ("far" depends on h_i), these boundary values will remain essentially constant, a circumstance that obtains for all the numerical simulations to be described below.

Spherically Averaged Reference State

We determine the radial dependence of ρ_r, p_r, g, and K_S (adiabatic bulk modulus) using PREM data [*Dziewonski and Anderson*, 1981], assume c_p to be determined by a thermal model [*Stacey*, 1977], and assume k to be determined by the experimental measurements of *Osako and Ito* [1991] for the lower mantle and of *Kieffer* [1976] for the upper mantle and transition zone. Each of these functions, excepting p_r, is represented numerically by three distinct curves, one fit to the lower mantle, f_{lm}, one fit to the transition zone, f_{tz}, and one fit to the upper mantle, f_{um}. These three curves are then combined as follows:

$$f = f_{lm} + (f_{tz} - f_{lm})g_2 + (f_{um} - f_{tz})g_1 \quad (29)$$

$$g_i = \tfrac{1}{2}[1 - \tanh((R_i - r)h_i)]$$

$$g_i = 0$$

if the ith phase boundary is not present.

Here R_1 corresponds to a depth of 400 km and R_2 corresponds to a depth of 670 km. Since p_r displays no large discontinuities, it is fit to a single curve over the entire extent of the mantle. This provides analytic representations for the reference state variables that well represent the spherically averaged depth variation of properties for the present-day Earth and are continuous at the depths of the two major phase changes.

The phase loop thicknesses are controlled by the parameters h_i. If a phase loop thickness δ_i is defined to be the depth range over which 95% of phase i changes to phase $i + 1$, then with the scaling here employed, we have the approximate relationship

$$\delta_i \text{ [in km]} \approx 10^4/h_i \text{ [nondimensional]}$$

for values of the parameters h_i used in these simulations. The largest values of h_i employed here are $h_1 = h_2 = 400$ which correspond to a phase loop thickness of 25 km. In the mantle, however, the actual phase loops are much narrower, particularly at the 670-km phase transition; for example, magnesian spinel dissociates into perovskite and magnesiowüstite at a pressure and temperature corresponding to 670 km depth over a pressure interval of less than 0.15 GPa (less than 4 km) [*Ito and Takahashi*, 1989]. Twenty-five kilometer

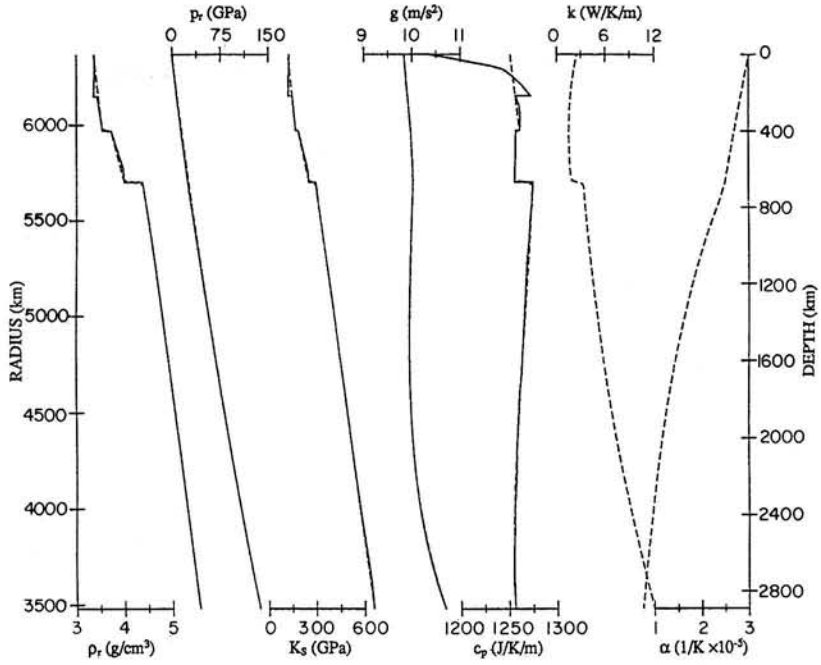

Figure 2. Pictoral representation of the data in Table 1 (dashed lines) together with function values given by PREM (solid lines) for ρ_r, p_r, g, and K_S and a thermal model by *Stacey* [1977] (solid line) for c_p. In some places the dashed line is not visible because it overlays the solid line.

phase loops are too broad to properly represent the major phase transitions in the mantle but are the narrowest phase loop thicknesses allowed at the highest numerical resolution achievable on the computers available to us. It is important to understand therefore the effect of changing phase loop thickness on the style of convection.

Three other functions must be specified for use in the model. The thermal diffusivity $\kappa = k/\rho_r c_p$ is known once k, ρ_r, and c_p are determined. The coefficient of thermal expansion is related to the density in a uniphase region as:

$$\alpha/\alpha_0 = (\rho/\rho_0)^{-\delta_T},$$
$$\delta_T = -\frac{1}{\alpha K_T}\left(\frac{\partial K_T}{\partial T}\right)_p = -\left(\frac{\partial \ln \alpha}{\partial \ln \rho}\right)_T, \quad (30)$$

if δ_T (the Anderson-Gruneisen parameter) may be assumed independent of pressure and temperature. *Anderson et al.* [1990] and *Reynard and Price* [1990] suggest that δ_T is, in fact, constant over significant compressions and temperature variations and that δ_T lies between 4 and 6 in the lower mantle. We have used (30) to determine α from ρ_r with $\delta_T = 5$ for the lower mantle and a linear variation in α across the upper mantle and transition zone from 2.5×10^{-5} K^{-1} at 670 km depth to 3.0×10^{-5} K^{-1} at the surface. The third function, the isothermal bulk modulus K_T, is related to the adiabatic bulk modulus K_S as

$$\frac{K_S}{K_T} = 1 + \frac{\alpha^2 K_S T}{\rho c_p}.$$

For a temperature ranging from 300 K at the surface to 4000 K at the CMB, K_S and K_T differ by a maximum of 5% but less than 1% over the majority of the mantle. In light of this, we shall set $K_S = K_T$ for the purpose of model calculations.

For ρ_r, g, K_S, and c_p the lower mantle data were fit to cubic expressions, while for the narrower transition zone and upper mantle the data were fit to straight lines. Because it displays no major discontinuities, the reference pressure p_r was fit to a cubic. Since there is greater variability in the radial dependence of thermal conductivity near the surface (as compared to the other reference state functions), all three constituent curves of k were cubic expressions. Table 1 lists the nondimensional coefficients along with the reference value for each depth dependent function required to characterize the anelastic basic state. Recalling that the radius is scaled by $d = 2.89 \times 10^6$ m allows one, with the information provided in Table 1, to determine dimensional and nondimensional values at any depth for any of the functions of the reference state. The reference state functions are also displayed in Figure 2 as dashed lines. The solid lines represent model data from either PREM [*Dziewonski and Anderson*, 1981] for ρ_r, p_r, K_S, and g or a thermal model by *Stacey* [1977] for c_p.

Results: Layered Flows and Their Temporal Stability

This section explores in detail the effects of varying the amount of internal heating and the Clapeyron slopes of both the 400-km and 670-km phase transitions. This discussion is preceded by a description of the quasi-periodicity that may be observed in the time dependence of partially layered flows that is the main new phenomenological result that our analyses have revealed. The range of values over which these parameters are varied has been chosen to match the range expected for these parameters in Earth's mantle. The Rayleigh number of Earth is near $Ra = 10^7$ [e.g., *Solheim and Peltier*, 1990], and all of the simulations described below

have therefore been performed for this value of the main control variable.

It is nevertheless of great interest to understand the effect of varying Ra on the propensity for layering in a given flow. Increasing the Rayleigh number, in fact, tends to increase the propensity for layering of a convective circulation when phase boundaries are present. This is understood to be a consequence of the greater phase boundary deflection induced by the larger temperature gradients that exist across sinking and rising plumes in the higher Rayleigh number fluid. Since it is the advection of ambient temperature across a phase boundary which is primarily responsible for the phase boundary deflection, plumes with a larger temperature gradient across them will produce larger deflections of the phase boundary. As explained in more detail below, greater phase boundary deflection at the endothermic 670-km transition results in a greater propensity for layering in the fluid. Increasing the Rayleigh number while keeping all other parameters unchanged therefore results in greater layering in the mantle. This is significant because, in the early Earth, the Rayleigh number was much higher than it is currently [*Sharpe and Peltier*, 1978]. This implies therefore that the degree of layering was quite likely much higher in the past than it is at present.

A diagnostic which will be employed below in order to quantify the degree of layering in a given flow is the relative radial mass flux diagnostic F_m that we define as follows:

$$F_m(r, t) = \frac{\langle \rho_r |u_r| \rangle}{[1/(r_{sur} - r_{cmb})] \int_{r_{cmb}}^{r_{sur}} \langle \rho_r |u_r| \rangle \, dr} \tag{31}$$

Here $\langle \rho_r |u_r| \rangle$ represents the absolute value of the mass flux averaged over a surface of constant radius. This is nondimensionalized by the globally averaged absolute mass flux such that

$$\int_{r_{cmb}}^{r_{sur}} F_m \, dr = 1.$$

The value of F_m at the surface and core-mantle boundary is always zero, and it is greater than zero between these boundaries. This results in a characteristic quasi-parabolic shape for F_m. In simulations which include phase boundaries at a depth (such as 670 km), where the average mass flux is reduced, a local minimum develops in the curve $F_m(r)$. The value of F_m at this local minimum is indicative of the degree of layering in the flow at a particular time. Thus this relative mass flux function is useful for quantifying the degree of layering in simulations which contain phase boundaries. Moreover, because F_m is normalized such that the area under it is always one, it may be used to make comparisons between simulations from different regions of parameter space. Its utility in this regard has been demonstrated previously [*Peltier and Solheim*, 1992; *Solheim and Peltier*, 1993].

Temporal Variability in Partially Layered Flows

Adjusting the parameters so that the physical configuration is "Earth-like", we inevitably discover the flow predicted by the model to exist in what we shall term a "partially layered" state (as previously noted in the very cursory analysis of both *Machetel and Weber* [1991] and *Peltier and Solheim* [1992]) that displays a very interesting characteristic time dependence. We begin this discussion by describing a simulation at a Rayleigh number of 10^7, with no internal heating, Clapeyron slopes of +3.0 MPa/K for the 400-km phase change and −2.8 MPa/K for the 670-km phase change, and phase loop thicknesses of 50 km at both the 400-km and 670-km phase boundaries. This simulation is employed to illustrate the nature of the time dependence in such Earth-like flows, a time dependence characterized by fluctuations between highly layered and essentially whole mantle styles of mixing. In this simulation and in all those discussed below the fractional density change across the olivine-spinel transition is 0.05 and across the spinel-postspinel transition it is 0.11.

Figure 3 displays the time dependence of the dimensional average absolute mass flux at the positions of the two phase boundaries (Figure 3c), average absolute surface velocity (Figure 3b), and average shell temperature (Figure 3a) for this simulation. Note that to obtain this and all subsequent time series, the model has been integrated from an initial state into a state of statistical equilibrium; the portion of the time integration containing the thermal transient characterizing the approach to this statistical equilibrium is always discarded, as explicitly discussed in our previous analysis of flows without phase transitions [*Solheim and Peltier*, 1990]. The most striking feature of these time series is the existence of a very long timescale transience. This transience is characterized by periods which begin with a sudden increase in mass flux at both 400 km and 670 km depths and a corresponding increase in surface velocity together with a sharply increasing average shell temperature. The mass flux and surface velocity then decrease sharply and hover near a minimum value for the remainder of the period. The average shell temperature reaches a maximum shortly after the maximum in average surface velocity is achieved, then gradually decreases for the remainder of the period. The peaks in mass flux imply a greater than average fluid velocity throughout the fixed volume, fixed mass mantle. This results in a high average surface velocity during these periods, as is apparent in Figure 3, as well as an associated higher than average surface heat flow. Conversely, periods of low radial mass flux at 400 km and 670 km depths correspond to periods of relatively low surface velocities. The high mass flux events are characterized by intense localized downwellings across the 670-km phase boundary that erupt and subside in a relatively short period of time. The upward moving return flow tends to be more diffuse than the downwellings during these "avalanche" events, although there are occasions when a strong rising plume is observed to cross into the upper mantle. After the initial avalanche of fluid across the 670-km phase boundary subsides, the flow returns to a dominantly layered style of convection in which the mass flux at 670 km almost vanishes (see Figure 3).

In order to understand this avalanche phenomenon more fully, Plate 1 includes a sequence of instantaneous temperature fields covering the period of time spanning one of these events. The six frames in Plate 1 are from the same simulation represented by Figure 3. The times at which these "snapshots" of the temperature field were taken are indicated on Figure 3 by the six vertical arrows attached to the top of Figure 3c. The actual times, relative to the start of the time series of Figure 3, are also indicated in Plate 1 beside

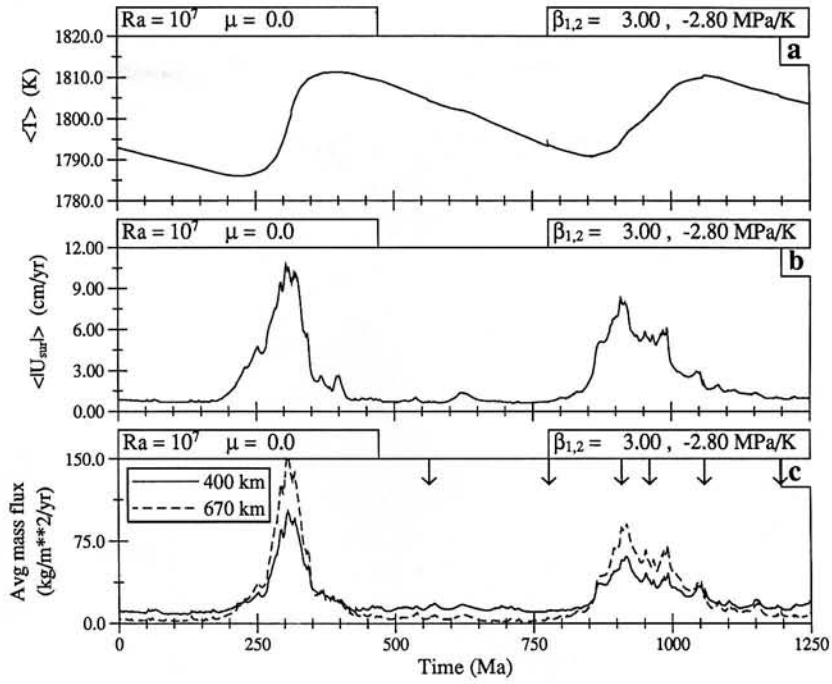

Figure 3. (a) Time series of the average mantle temperature, (b) average absolute surface velocity, and (c) dimensional average absolute mass flux at the positions of the 400-km and 670-km phase boundaries. All three time series come from a simulation in which $Ra = 10^7$, $\mu = 0$, $\beta_1 = +3.0$ MPa/K, $\beta_2 = -2.8$ MPa/K, and $h_1 = h_2 = 200$. The long time scale variation associated with the presence of phase boundaries in this configuration of model parameters is clearly evident in these time series. The arrows in Figure 3c indicate the times for the temperature fields of Figure 4.

each frame. The first two frames of this sequence (562 Ma and 780 Ma) come from a time when the flow is highly layered. There is a large number of small-scale convection cells operating in the upper mantle at this time and a few larger-scale cells in the lower mantle. An enlarged version of the 780 Ma plot is reproduced (Plate 2) as representative of the highly layered period and a more detailed discussion of it will follow. We shall first comment here on the manner in which the flow evolves through a representative avalanche event. The 910 Ma frame shows the temperature field at the time when the 670-km mass flux is at its peak (see Figure 3). Even though this is the time at which the azimuthally integrated 670-km mass flux is greatest, there are only two locations apparent where the mass flux across 670 km depth is significant; that is, at the "north" pole and at a point two thirds of the way toward the "south" pole. At both of these locations, the flow is descending. Obviously, there is a return flow, but the return flow is much more diffuse and so is not nearly so apparent in the pattern of isotherms. Fluid is returning to the surface in the region midway between the two major descending plumes, resulting in two massive convection cells that extend the depth of the mantle and cover a horizontal extent spanning two thirds of the shell. There is third large cell that operates between the "south" pole and a point roughly 60° distant, but the associated deep circulation is inhibited by the fact that the flow remains layered in the vicinity of the "south" pole. Thus the flow exhibits a quasi-three-cell pattern at the time of the peak 670-km mass flux that is dominated by two intense downwellings. This pattern persists to the next frame. The 960 Ma field is similar to this, although there is some indication that the downwelling that exists two thirds of the way between the "north" and "south" poles is beginning to subside. By the next frame (1060 Ma) the downwelling at the "north" pole has collapsed almost completely and a rising polar plume is emerging from the bottom boundary layer. The other major sinking plume is still present but is also diminished significantly. At the same time the many minor plumes that were rising from the lower thermal boundary layer between the two major sinking plumes have grouped together and have formed a single upwelling that is more intense than any of the now amalgamated constituent plumes. By the last frame (1196 Ma) both of the previously dominant descending plumes have been cut off completely at the 670-km boundary. A new downwelling has emerged near the "south" pole, but across most of the latitudinal extent of the 670-km boundary there is little mass flux and the fluid is once again in a highly layered state.

The extent to which the flow is dominated by the two downwelling plumes is usefully quantified by the ratio of maximum downward radial velocity to maximum upward radial velocity at a particular point in time. This ratio is 4.5 for the 910 Ma flow of Plate 1 at the time of peak 670-km mass flux. In comparison, the ratio is very nearly unity for both the 562 Ma and 780 Ma flows, it decreases to 2.5 for the 960 Ma flow and is near unity again for both the 1060 Ma and 1196 Ma flows. This further indicates that the high 670-km mass flux events are dominated by intense downwellings. As we have seen these avalanches of fluid across the 670-km phase boundary onset very abruptly and violently. They

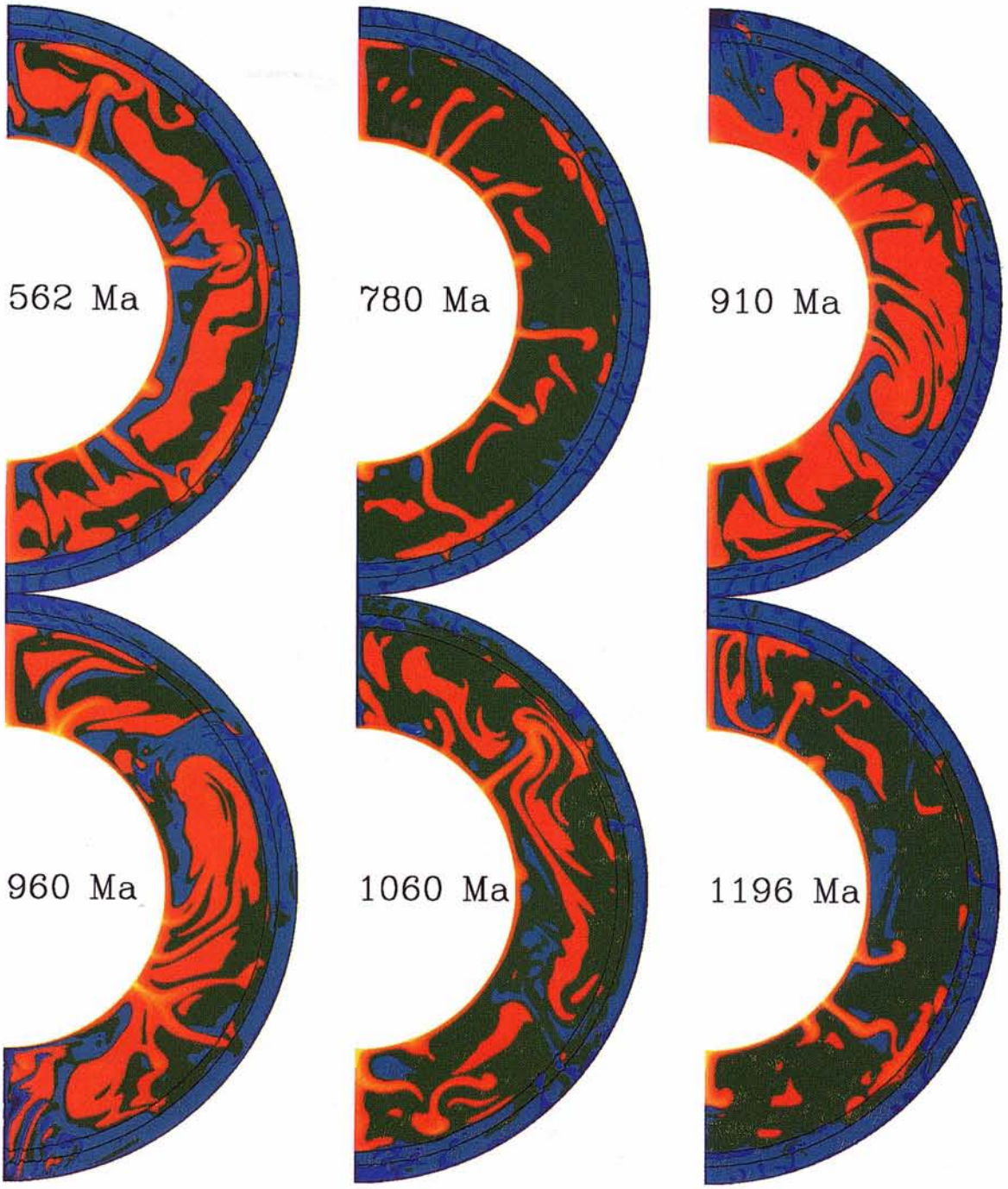

Plate 1. Sequence of isotherms showing the variation in the flow as it goes through an "avalanche" event. These times correspond to the time in Fig. 3 and the exact position of each temperature field in this sequence is indicated in frame c of Fig. 3 by the vertical arrows pointing down from the top of the frame.

transform a highly layered flow into a flow which is essentially whole mantle in style, although there may be pockets of layering that persist throughout the event. As quickly as these avalanches begin, however, the major descending plumes crossing the 670-km boundary are cut off and the fluid returns to its former layered state. The detailed physics of the mechanism responsible for this characteristic behavior is discussed below.

Another useful piece of information that may be derived from Figure 3 concerns the extent to which the instantaneous geotherm (the depth dependent azimuthally averaged temperature) deviates from the time average geotherm. Several time-averaged geotherms are presented below, and in the discussion of these, one should always bear in mind that any particular instantaneous profile will differ slightly from the average. The differences between instantaneous and time-averaged profiles occur primarily in the interior region away from the thermal boundary layers and are manifest as shifts of the temperature of this central core to higher or lower values. In the time series of average shell temperature in Figure 3, the minimum average temperature is 1786 K and the maximum average temperature is 1811 K.

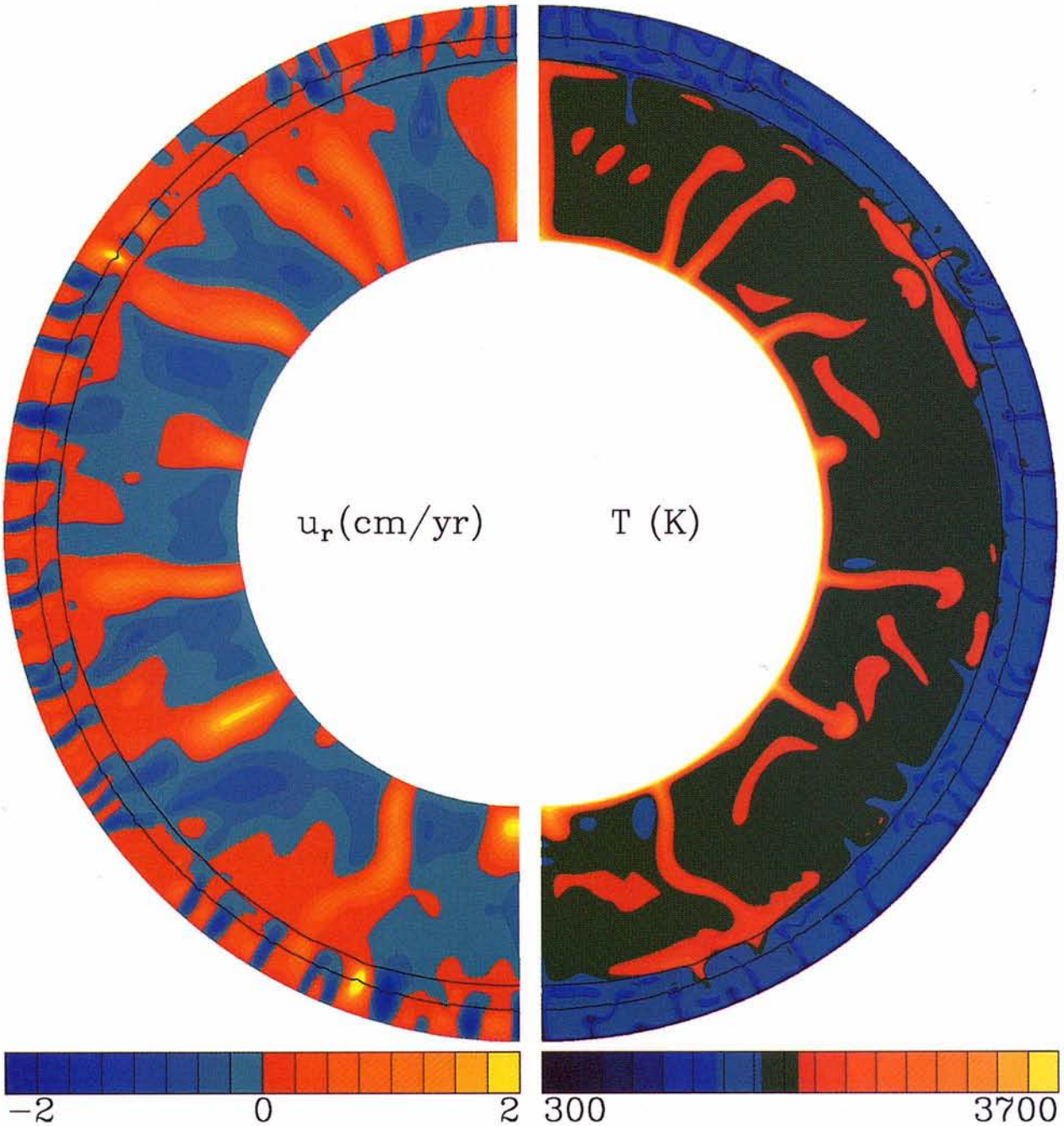

Plate 2. A "snap-shot" of isotherms (right) and radial velocity contours (left) from the simulation of Fig. 3 at a time of 780 Ma showing the structure of the flow when it is in a highly layered state.

Variations in the average shell temperature correspond to shifts in the temperature characteristic of the geotherm core. A total variation in the average shell temperature of roughly 30 K therefore corresponds to a shift of the instantaneous temperature in the geotherm core by ±15 K. This is roughly the magnitude of shifts in the instantaneous geotherm away from the time average that are characteristic of all of these simulations.

It is often informative to view "snapshots" of the temperature field (as in Plate 1) or of some other field from these simulations in order to develop some understanding of what constitutes typical structures in these flows. In Plate 2 we show the contoured temperature field on the right and radial velocity on the left for a flow from this simulation at the time of 780 Ma. This corresponds to a time following completion of a cycle in which the flow is highly layered but when an avalanche event is just about to occur (see Figure 3). The two curves, one dashed and one dotted, running parallel to the surface and slightly below it, represent the positions of the 400-km and 670-km phase boundaries, respectively. Negative (dashed line) contours in the velocity plot represent downward moving fluid, while positive (solid line) contours represent upward moving fluid. It is clear from both these diagrams that there is little mass transfer across the

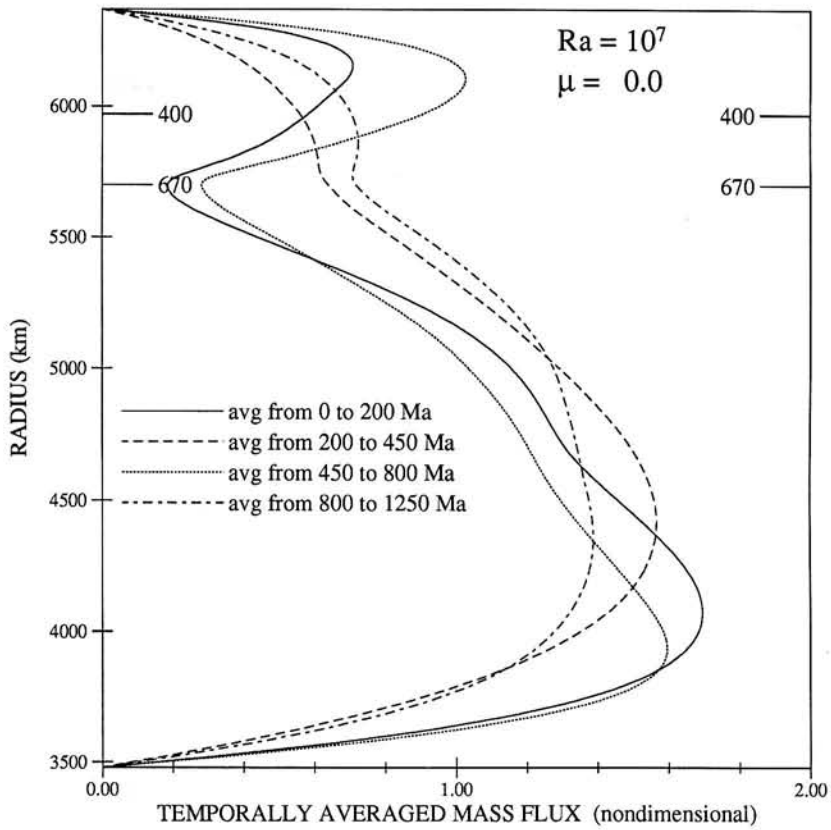

Figure 4. F_m averaged over four different time periods from the simulation of Figure 3. This provides a clear indication that in this simulation there are periods when the flow is highly layered as well as periods when there is high mass flux across the 670-km phase boundary. As mentioned in the text these flows may be characterized as statistically stationary only when averaged over sufficient long time.

670-km phase boundary. It is also clear from both these diagrams that there is little mass transfer across the 670-km phase boundary. It is also clear that the scale of the convection cells in the upper mantle are markedly smaller than those in the lower mantle. There are some 25 to 30 cell pairs in the upper mantle while there are only eight in the lower mantle at this particular instant of time. Most of the cells are operating with an aspect ratio less than 1, both in the lower and upper mantle. There is one notable exception to this general rule, however. A very large aspect ratio cell will be seen to exist in the upper mantle near 2 o'clock and 10 o'clock in the complementary images of Plate 2. This is typical of the flow pattern that develops following one of the avalanche events described above. There are a great many small aspect ratio cells operating in the fluid, and the flow is highly layered.

The extent of the layering over various parts of a cycle may be determined using the mass flux diagnostic F_m. Figure 4 presents the temporal average of F_m over four separate time segments of this simulation. The time series of Figure 3 has been subdivided into four segments: 0–200 Ma, 200–450 Ma, 450–800 Ma, and 800–1250 Ma, and F_m is averaged over each period individually. These four functions are plotted in Figure 4. The time periods from 0–200 Ma and 450–800 Ma display significant layering, while during the other two time periods there is very little layering. Figure 4 corroborates and verifies the previous assertion that in this region of parameter space, the flow spends alternate periods of time in a highly layered state and in a whole mantle state. In neither of these states is the flow perfectly layered nor perfectly whole mantle in style. Rather there is a spatial nonuniformity of layering in which plumes cross the 670-km phase boundary in some locations, but elsewhere along this boundary there is essentially no radial mass transfer. The number and intensity of plumes that do traverse this boundary fluctuate in time. This characteristic behavior was alluded to previously by *Solheim and Peltier* [1993], but it was not nearly so evident. This suggests that this behavior is indeed typical of a flow as it approaches a layered regime from an unlayered regime through variation of model parameters such as h_i, Ra or β_i. It should be noted that these episodically layered flows are statistically stationary only when the averaging timescale is sufficiently long.

Impact of Individual Phase Boundaries on Radial Mixing

Both the effect of latent heating and the effect of phase boundary deflection are factors which influence the flow of fluid through a phase boundary as originally discussed by *Busse and Schubert* [1971] from the perspective of linear stability analysis. Thermal expansion of downward moving fluid, due to latent heat release, at an exothermic phase boundary, for example, will result in an added positive buoyancy and therefore will tend to reduce the vigor of descending flow. Conversely, thermal contraction, due to latent heat absorption, of downward moving fluid at an endothermic phase transition will result in an added negative buoyancy and tend to accelerate the flow of fluid across the

transition. It is clear on a priori grounds that the endothermic transition tends to cause phase boundary deflection in the direction of the fluid flow across it, whereas the exothermic transition causes phase boundary deflection in a direction opposite to the fluid flow. Consequently, a column of sinking fluid crossing the exothermic transition would contain more of the heavy phase, relative to the ambient fluid, and thus experience an added downward force. A sinking column crossing the endothermic transition, however, would contain relatively more of the light phase and thus experience an upward force. Similar reasoning applies to rising fluid, and we see that latent heating and phase boundary deflection have opposite effects at both exothermic and endothermic phase transitions. In the linear regime, at a Rayleigh number corresponding to the onset of convection, the latent heating effect dominates [*Peltier*, 1985; *Peltier et al.*, 1989] and an exothermic transition would tend to inhibit convection whereas an endothermic transition would enhance convection. This is actually opposite to the original predictions of *Schubert et al.* [1975] whose calculations were improperly scaled, as pointed out by *Peltier* [1985]. At sufficiently high Rayleigh number one expects that the influence of phase boundary deflection will eventually overwhelm the effect of latent heat release as the latter should increase as $Ra^{2/3}$ (i.e., proportional to vertical velocity), whereas the former should increase as Ra (i.e., proportional to the lateral temperature heterogeneity in downwelling plumes). The results of the initial simulation described above demonstrate that the "Earth-like" Rayleigh number of 10^7 is sufficiently high that the endothermic 670-km horizon is already controlling the radial mixing.

We describe one further measure of the degree of layering in such flows. This is a single number that when it is zero implies there is no layering, when it is between zero and one implies that there is some degree of layering (one implies perfect layering), and when it is negative implies that the 670-km mass flux is greater than normal. Using the dimensional value for the 670-km absolute mass flux of 43.9 kg/m^2/yr from the no phase boundary simulation as a reference, we can define a number (P_0 say) defined as

$$P_0 = 1 - \frac{\text{670 km mass flux (kg/m}^2\text{/yr)}}{43.9},$$

that has these properties. The subscript zero indicates that the reference value that was used came from the $\mu = 0$ no phase boundary case. As we will see in the next section, this reference value changes as μ changes. The values of P_0 for four cases are listed in Table 2. These four cases correspond to simulations with two phase boundaries present, only one phase boundary at 400 km present, only one phase boundary at 670 km present, and no phase boundaries present. For comparison sake, dimensional values of both the 400-km and 670-km absolute mass flux from these same four simulations are presented as well. These values of P_0 give clear indication that the 670-km phase boundary tends to induce layering, while the 400-km phase boundary tends to promote increased radial mass flux. In combination, the two phase boundaries can, at least in this instance, produce a flow in which there is some degree of layering but for which the degree of layering is diminished from the 670-km phase boundary only case.

Table 2. Values of the Layering Parameter P_0 for Four Cases

	Mass Flux, km m^{-2} yr^{-1}		
	400 km	670 km	P_0
Two phase boundaries present	30.0	33.8	0.23
670-km phase boundary only	25.5	27.0	0.38
400-km phase boundary only	34.1	49.4	−0.13
No phase boundaries	31.6	43.9	0.00

Also included are the average values of the dimensional absolute mass flux at 400 km and 670 km.

Influence of Internal Heating on the Propensity for Layered Flow

To this point in the analysis, all of the simulations discussed have been characterized as having no internal heating. Since there is likely significant internal heating in Earth's mantle due to the decay of long-lived radionucleides such as ^{235,238}U, ^{232}Th, and ^{40}K, it is important to understand the influence of adding internal heating on such flows. The most obvious effect of the addition of internal heating to the mantle is to raise its average temperature. This effect is evident in Figure 5. Figure 5 shows the temporally averaged geotherms for four simulations. The solid and the dotted curves represent geotherms from two simulations in which there are no phase boundaries in the fluid and the Rayleigh number is 10^7. These two simulations differ only in the fact that one contains no internal heating (solid curve) and one contains internal heating corresponding to $\mu = 10$ (dotted curve). The dashed and the dashed-dotted curves represent geotherms from two simulations which contain both phase boundaries with $\beta_1 = +3.0$ MPa/K and $\beta_2 = -2.8$ MPa/K. The dashed curve corresponds to results from a simulation that has phase loop thickness parameters $h_1 = h_2 = 200$, while the dashed-dotted curve is for a simulation that has phase loop thickness parameters $h_1 = h_2 = 400$. The effect of changing h_i over this range is small and is discussed below. Clearly, the first-order effect of adding internal heating is to increase the core temperature of the geotherm as the temperature drop across the upper and lower thermal boundary layers adjusts to the altered heat distribution. The net effect is to raise the average temperature of the mantle. For the simulations with no phase boundaries, the overall average temperature for the $\mu = 0$ case is 1680 K, while the overall average temperature for the $\mu = 10$ case is 2078 K, a difference of 398 K. For the simulations with phase boundaries included, the average overall temperature for the $\mu = 0$ case is 1800 K and the average overall temperature for the $\mu = 10$ case is 2200 K, a difference of 400 K. Therefore adding this amount of internal heating raises the average temperature of the mantle by around 400 K. The increase in temperature is characterized by a shift of the geotherm core to higher temperatures, but the shape of the geotherm is not altered. It is apparent from Figure 5 that adding internal heating does not affect the average temperature gradient across the mantle. Nor does it influence, qualitatively, the internal thermal boundary layer that exists at 670 km or the abrupt change in slope that exists at 400 km (in the simulations with both phase boundaries present).

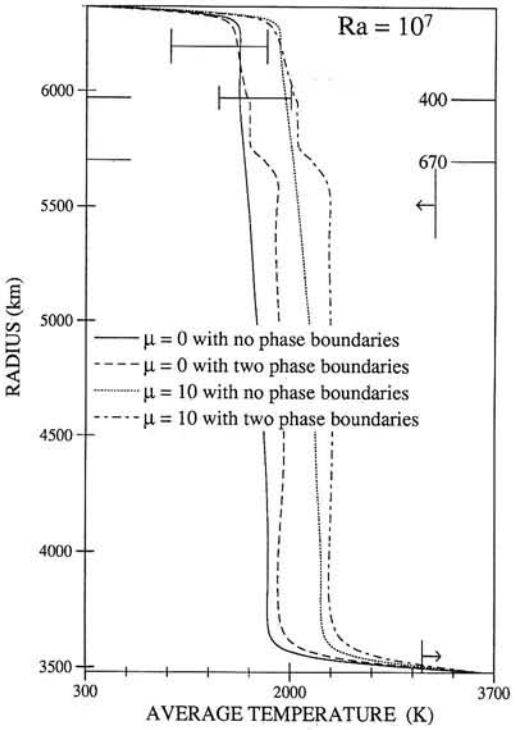

Figure 5. Effect of internal heating on the temporally averaged geotherm. All four geotherms shown are from simulations with a Rayleigh number of 10^7. The solid and the dotted curves are from simulations in which there are no phase boundaries, while the other two curves come from simulations in which both phase boundaries are present with $\beta_1 = +3.0$ MPa/K and $\beta_2 = -2.8$ MPa/K. The two curves on the right come from simulations in which there is internal heating corresponding to $\mu = 10$. The most obvious effect of adding internal heating is to raise the average temperature of the mantle by increasing the temperature characteristic of the geotherm core ($\approx$400 K for these cases). The error bars and vertical lines with attached arrows represent constraints on an "Earth-like" geotherm as discussed in the text.

A useful additional piece of information that may be determined from these geotherms is the ratio of internal heating to total heating from within and below (the Urey ratio). Note that this is not μ (except when $\mu = 0$) in these simulations, as it was in the uniphase model [*Solheim and Peltier*, 1990] due to the fact that both the upper and lower boundaries are taken to be isothermal in the multiphase model. This ratio is determined by calculating the time averaged heat flux across the cmb and across the surface, taking the difference and dividing by the surface heat flux. In this fashion we have determined this ratio to be 0.04 for the solid curve of Figure 5 ($\mu = 0$), 0.02 for the dashed curve ($\mu = 0$), 0.42 for the dotted curve ($\mu = 10$) and 0.53 for the dashed-dotted curve ($\mu = 10$). One would expect that in the time average, this ratio would be zero for the $\mu = 0$ cases. The fact that it is not exactly zero here indicates either that the average has not been taken over a sufficiently long period of time or that the flow still retains remnant heat from the initialization. In either case it is very nearly zero. The more interesting numbers are for the $\mu = 10$ cases; $\mu = 10$ corresponds to roughly 50% heating from within, according to the values given above, determined from the geotherms of Figure 5. A value of $\mu = 10$ translates to an internal heating rate per unit mass of 10^{-11} W/kg using the definition of μ (equation (13)), values from Table 1, and the fact that $Ra = 10^7$ (meaning that $T_c = 3314.3$ K). Using a density of $\rho_0 = 4 \times 10^3$ kg m^{-3}, this constant heating per unit mass translates into a constant heating rate per unit volume of 4×10^{-8} W m^{-3}. This is, of course, only an approximate value since the internal heating rate is in fact constant per unit mass in the multiphase model, but a number is required for comparison with estimates of the amount of internal heating in the actual Earth. A typical estimate of the radioactive heating rate in the Earth is 2×10^{-8} W m^{-3} [*Jeanloz and Morris*, 1986]. From this perspective therefore, $\mu = 10$ is a reasonable value, if not somewhat high. If we assume a value of $\mu \leq 10$, then we must accept a ratio of internal heating to heating from within and below $\leq$0.50. This ratio is at the extreme lower limit of most current estimates which range from 0.5 [*Davies*, 1980] to 0.9 [*Turcotte*, 1980] based on the parameterized convection ideas developed by *Sharpe and Peltier* [1978, 1979]. The higher value of 0.9 has generally been preferred in the most recent literature. If the quasi-steady state analyses that are under discussion here are relevant to the secularly cooling planet, then this currently preferred value is excessive.

There do, of course, exist direct constraints on the mantle geotherm from high-pressure experiments such as those used to determine the phase diagram of its constituent silicate mineralogy as well as from experimental constraints on the melting temperature of iron at the core-mantle boundary. Figure 5 incorporates constraints on the geotherm derived from various sources. In the upper mantle, temperatures of 1000–1800 K occur at depths ranging from 100 to 250 km. This is indicated by the error bars at this depth in Figure 5. These temperatures are determined from the study of xenoliths brought up volcanically from these depths in the mantle as reviewed, for example, by *Jeanloz and Morris* [1986]. The temperature at the top of the transition zone at 400 km depth may also be bracketed by determining the range of temperatures over which the olivine-spinel transition can take place at the pressure corresponding to this depth. This estimate suggests an absolute temperature of 1700 $\pm$ 300 K at 400 km depth [*Jeanloz and Thompson*, 1983]. The temperature at the top of the lower mantle cannot be greater than the melting point of perovskite at pressures typical of this depth. The melting point of $(Mg_{0.9}Fe_{0.1})SiO_3$ perovskite was found to be 2600–3200 K [*Jeanloz and Heinz*, 1984]. A maximum temperature for the top of the lower mantle is then 3200 K as indicated on Figure 5. The core-mantle boundary temperature can be constrained by the melting point of the iron-dominated liquid that makes up the outer core. High-pressure measurements of the melting of appropriate iron mixtures place the CMB temperature at 3600 $\pm$ 500 K [*Brown and McQueen*, 1986]. This estimate is also indicated on Figure 5. One can see from Figure 5 that a value of $\mu = 10$ puts the geotherm above the upper limit of these constraints (at least of the ones in the upper mantle) and increasing the value of μ would push the geotherm farther outside these limits. On the basis of this evidence we would have to say that $\mu = 10$ is the largest value of μ permissible for an "Earth-like" mantle. This would also seem to indicate therefore that the Urey ratio is no greater than $\approx$0.5 if the assumption that heat flow may be considered quasi-static is valid.

Another well-known effect of adding internal heating is that the vigor of hot plumes rising from the CMB is diminished in favor of cold plumes sinking from the surface. A consequence of this added relative importance of cold plumes sinking from the upper thermal boundary layer is an increased propensity for layering as internal heating is added to the fluid. A line of physical argument that makes this fact understandable is as follows:

1. It is the magnitude of the deflection of the 670-km phase boundary away from its average depth that determines the degree of layering.
2. It is the advection of ambient temperature across 670 km that is primarily responsible for this deflection.
3. Cold sinking plumes from the surface have a larger temperature gradient across them in a fluid with internal heating than in a fluid without internal heating due to the hotter mantle interior (Figure 5) and so produce a greater phase boundary deflection.
4. Because the 670-km boundary is much nearer to the surface than the core-mantle boundary, there will be more cold plumes from the surface reaching 670 km than hot plumes from the CMB. This implies that although adding internal heating decreases the temperature gradient across hot rising plumes and thus decreases the magnitude of phase boundary deflections caused by them, the net effect of adding internal heating is to increase the magnitude of the 670 km phase boundary deflections in the regions of descending flow that control mixing.

Two simulations with Rayleigh number of 10^7, $\beta_1 = +3.0$ MPa/K, $\beta_2 = -2.8$ MPa/K, and $h_1 = h_2 = 200$ were performed, one with no internal heating and one with internal heating corresponding to $\mu = 10$. A value of the layering parameter P_0 for the $\mu = 0$ case was determined to be 0.32. The layering parameter P_{10} for the $\mu = 10$ simulation was determined to be 0.50. Since larger values of the layering parameter mean a greater degree of layering, it is apparent that increasing the amount of internal heating from $\mu = 0$ to $\mu = 10$ does indeed increase the propensity for layering in the fluid.

Dependence of the Extent of Layering on the Clapeyron Slope of the Spinel-Postspinel Transition

In order to understand the impact of varying the value of the 670-km Clapeyron slope we will describe geotherms and mass flux functions from two sets of simulations. The first set of simulations all have a Rayleigh number of 10^7, $\mu = 0$, $\beta_1 = +2.0$ MPa/K, and $h_1 = h_2 = 50$. The flows in this sequence differ only in the value of the 670-km Clapeyron slope; β_2 varies from -2.0 to -4.0 MPa/K with intermediate values of -2.5, -2.8, -3.2, and -3.6 MPa/K. Figure 6 shows time averaged geotherms from three of these simulations, $\beta_2 = -2.0$ MPa/K (solid line), $\beta_2 = -2.8$ MPa/K (dashed line), and $\beta_2 = -4.0$ MPa/K (dotted line). Figure 7 shows the mass flux function F_m for all simulations in this sequence. Decreasing the value of the 670-km Clapeyron slope from -2.0 to -4.0 MPa/K in these simulations drives the flow from an essentially unlayered state to a strongly layered state. This is evident in both Figures 6 and 7. In Figure 6 we see the appearance of an internal thermal boundary layer in the $\beta_2 = -4.0$ MPa/K time-averaged geotherm. A small 670-km thermal boundary layer is evident in all three geotherms, but the magnitude of the temperature drop across it increases with decreasing β_2. It is really only

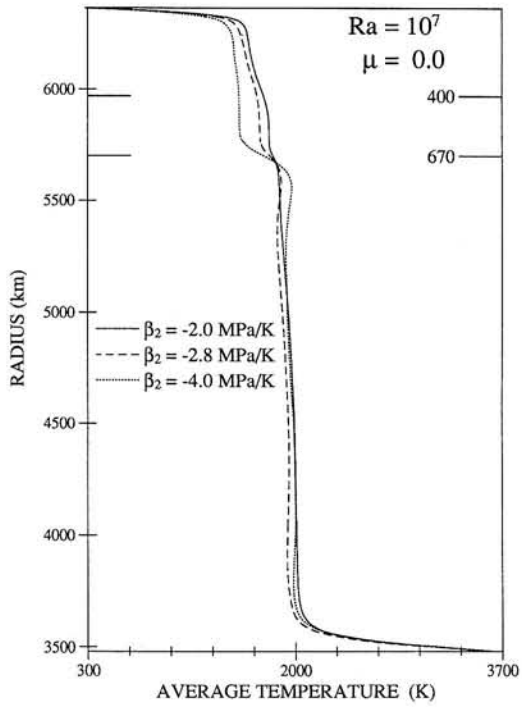

Figure 6. Time-averaged geotherms from three simulations at a Rayleigh number of 10^7 with no internal heating. These flows all have two phase boundaries present ($h_1 = h_2 = 50$) with the Clapeyron slope of the 400-km phase change being +2 MPa/K. The three flows differ only in the value of the 670-km Clapeyron slope, the three values being -2.0, -2.8, and -4.0 MPa/K as indicated. As the Clapeyron slope of the 670-km phase boundary decreases, an internal thermal boundary layer develops at 670 km.

the $\beta_2 = -4.0$ MPa/K simulation in which the boundary layer is fully developed. In Figure 7 the 670-km dip in the relative mass flux curves grows steadily as the value of β_2 decreases from -2.0 to -4.0 MPa/K. This implies, of course, that the relative mass flux at 670 km decreases, on average, as the Clapeyron slope of the 670-km phase boundary decreases. This fact, coupled with the fact that a substantial internal thermal boundary layer develops at 670 km as β_2 decreases, indicates that the magnitude of the 670-km Clapeyron slope is an important factor, perhaps the most important factor, in determining the degree of layering in a particular flow.

We may quantify the degree of layering using time averaged values of the absolute mass flux at 670 km. We have determined values of the layering parameter P_0 for this set of simulations. These values are given in Table 3. P_0 ranges from 0.07 for the $\beta_2 = -2.0$ MPa/K simulation to 0.53 for the $\beta_2 = -4.0$ MPa/K simulation. A value of $P_0 = 0.50$ implies that, on average, the 670-km mass flux is only 50% of the value it would be if no phase boundaries were present. The flow is far from steady, however. Because of the magnitude of fluctuations in F_m (670 km) a value of $P_0 = 0.53$ implies significant layering in the flow ($P_0 \geq 0.5$) about half the time. When making reference to the real Earth, the instantaneous flow structure is what is important. In a simulation in which $P_0 = 0.5$ the instantaneous flow structure is as likely to be highly layered as it is to be unlayered.

The nature of the time dependence of the radial mass flux

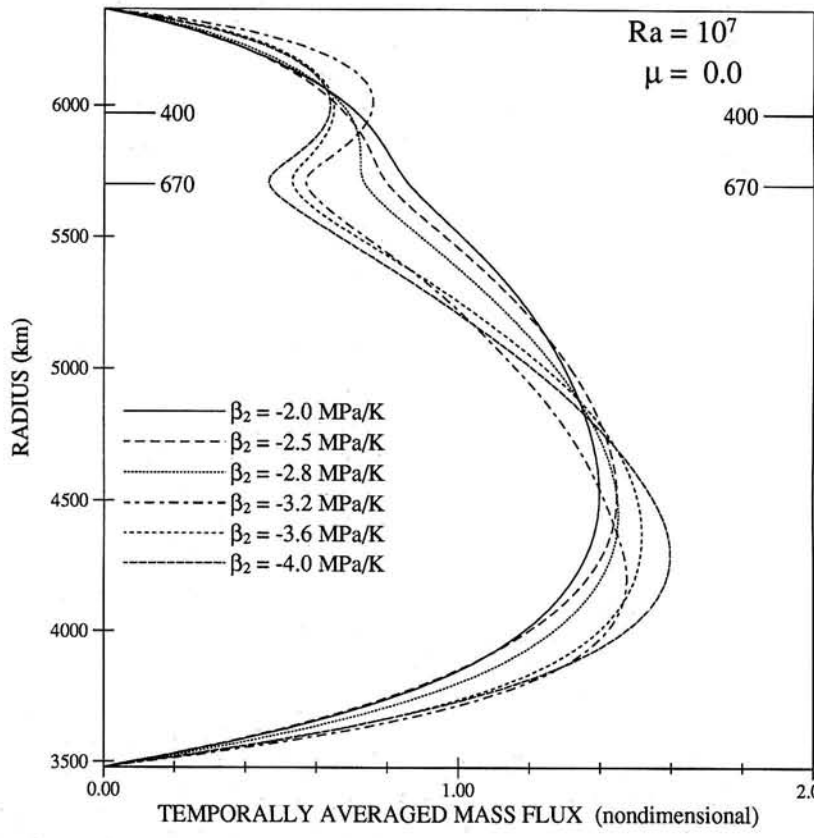

Figure 7. Comparison of the temporaly averaged mass flux function F_m from six different simulations at a Rayleigh number of 10^7 with no internal heating. In all simulations both phase boundaries were present ($h_1 = h_2 = 50$) with the Clapeyron slope of the 400-km phase boundary being +2 MPa/K. These simulations differ only in the value of the 670-km Clapeyron slope. The values of β_2 range between −2.0 and −4.0 MPa/K as indicated. This figure clearly shows that as the Clapeyron slope of the 670-km phase change decreases, the propensity for layering in the flow increases.

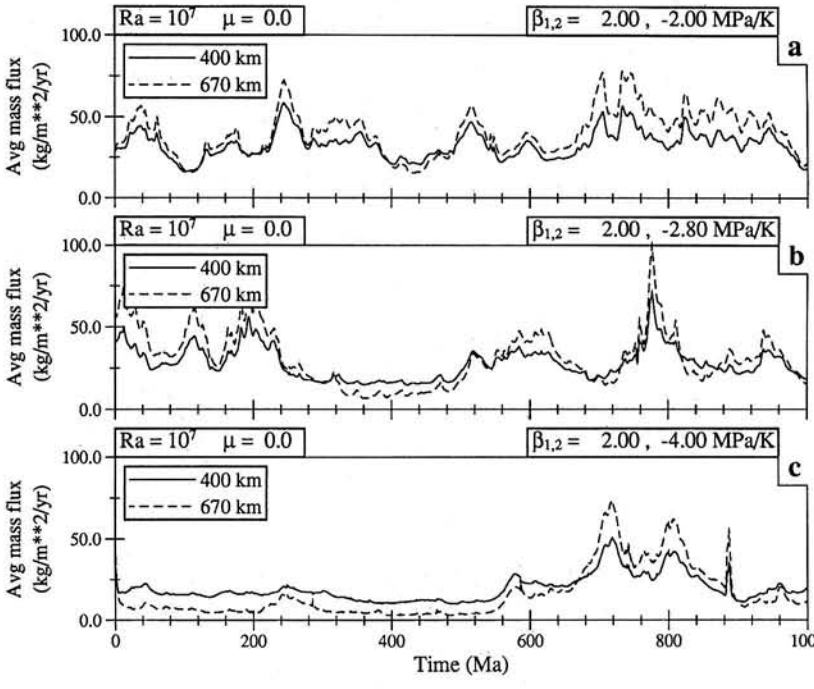

Figure 8. Time series of the (dimensional) spatial average of the absolute value of the mass flux at the position of the 400-km (solid line) and 670-km (dashed line) phase boundaries. All three time series come from simulations in which the Rayleigh number is 10^7, there is no internal heating, and the 400-km phase boundary has a Clapeyron slope of +2 MPa/K ($h_1 = h_2 = 50$). The time series in Figure 8a comes from a simulation in which the Clapeyron slope at 670 km is −2 MPa/K, in Figure 8b the 670-km Clapeyron slope is −2.8 MPa/K, and in Figure 8c the 670-km Clapeyron slope is −4.0 MPa/K. The decrease in mass flux at 670 km with a decrease in the 670-km Clapeyron slope is clearly evident in these time series.

at 400 km and at 670 km in this set of solutions is portrayed in Figure 8. Figure 8 shows time series of the variation of the 400-km and 670-km dimensional absolute mass flux for the same three simulations from which the time-averaged geotherms of Figure 6 were determined. Figure 8a is for the flow with a 670-km Clapeyron slope equal to −2.0 MPa/K; for Figure 8b, $\beta_2 = -2.8$ MPa/K, while for Figure 8c, $\beta_2 = -4.0$ MPa/K. These three time series show the characteristic behavior of the mass flux from three simulations which are essentially unlayered (Figure 8a), partially layered (Figure 8b), and very significantly layered (Figure 8c). In Figure 8a the 670-km mass flux spends virtually all of its time above the 400-km mass flux, indicating that there is little, if any, time in which the flow could be said to be layered. In Figure 8b there is at least one period of time (from about 300 Ma to 500 Ma) during which the flow is layered. The rest of the time the 670-km mass flux is rising and falling in bursts. These bursts of mass flux at 670 km correspond to localized "avalanches" of fluid across the 670-km phase boundary as previously described. In Figure 8c the fluid is in a layered state for the majority of the time (the time during which the 670-km mass flux is near zero and well below the 400-km mass flux). It recovers from the layered state for a relatively short period (from about 600 Ma to 900 Ma) and then returns. As the flow shifts into a region of parameter space in which there is a greater propensity for layering, the time dependence of certain functions (such as the average absolute mass flux at 400 km or 670 km depth as well as Nusselt number, surface velocity, and total kinetic energy) undergoes a characteristic change similar to that which we see in the three time series presented in Figure 8.

A second set of simulations was performed in which the parameters were set to more "Earth-like" values. These three simulations all have a Rayleigh number of 10^7, $\mu = 10$, $\beta_1 = +3.0$ MPa/K, and $h_1 = h_2 = 400$ (25-km phase loops). They differ only in the value of the 670-km Clapeyron slope which varies from $\beta_2 = -1.4$ MPa/K through $\beta_2 = -2.1$ MPa/K to $\beta_2 = -2.8$ MPa/K. Figure 9 displays the time-averaged geotherms and Figure 10 shows the relative mass flux functions for these three cases. The solid lines in both figures represent the $\beta_2 = -1.4$ MPa/K simulation, the dashed lines represent the $\beta_2 = -2.1$ MPa/K simulation, and the dotted lines represent the $\beta_2 = -2.8$ MPa/K simulation. The flow goes from an unlayered flow for the $\beta_2 = -1.4$ MPa/K case to a layered flow for the $\beta_2 = -2.8$ MPa/K case. This fact is apparent in Figures 9 and 10. In Figure 10 the value of F_m at 670 km decreases significantly from the $\beta_2 = -1.4$ MPa/K case to the $\beta_2 = -2.8$ MPa/K case, indicating a substantial increase in the degree of layering. This decrease in F_m (670 km) coupled with the existence of an internal thermal boundary layer at 670 km, apparent in the $\beta_2 = -2.8$ MPa/K geotherm of Figure 9, clearly demonstrates that there is significant layering in the $\beta_2 = -2.8$ MPa/K simulation. Therefore the effect of decreasing the value of the 670-km Clapeyron slope is to increase the propensity for layering in these simulations. This is in agreement with the above set of results from the $\mu = 0$ model, in which β_1 was +2.0 MPa/K and there were 200-km-thick phase loops. Table 4 gives dimensional values of the average absolute mass flux at 400 km and at 670 km that have been determined from the time series of these three simulations along with the calculated value of the layering parameter P_{10}. Although the range of β_2 is narrower for this set of three simulations than the previous set of six, the change in the layering parameter is greater. This greater sensitivity to the value of β_2 of the layering parameter is not all that surprising when one recalls that thinner phase loops (25 km versus 200 km), larger negative 670-km Clapeyron slope, and added internal heating ($\mu = 0$ versus $\mu = 10$) all increase the propensity for layering in the flow. A larger

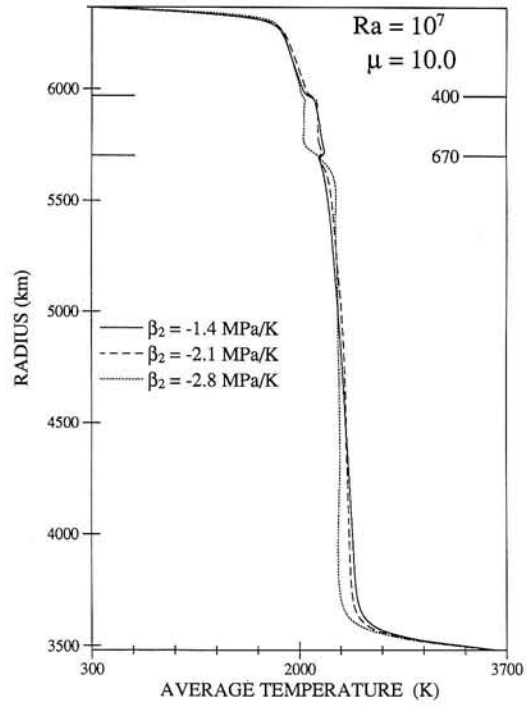

Figure 9. Geotherms showing the effect of decreasing the 670-km Clapeyron slope over a range through which the flow moves from a nonlayered regime to a layered regime. All three curves are from simulations with a Rayleigh number of 10^7, internal heating corresponding to $\mu = 10$, $\beta_1 = +3.0$ MPa/K and $h_1 = h_2 = 400$. The only difference between each of these runs is in the value of the 670-km Clapeyron slope; β_2 varies from −1.4 MPa/K representing a flow with no tendency toward layering to −2.1 MPa/K to −2.8 MPa/K representing a flow with significant layering (compare Figure 10).

Table 3. Values of the Layering Parameter P_0 for Six Simulations That Vary Only in the Value of the Clapeyron Slope at 670 km

	Mass Flux, km m^{-2} yr^{-1}		
β_2, MPa/K	400 km	670 km	P_0
−2.0	33.7	40.7	0.07
−2.5	30.1	36.7	0.16
−2.8	30.0	33.8	0.23
−3.2	25.9	27.4	0.38
−3.6	24.2	22.2	0.49
−4.0	22.5	20.6	0.53

The dimensional values of the 400 km and 670 km average absolute mass flux are included. $\mu = 0$; $\beta_1 = -2.0$ MPa/K; 200 km phase loops.

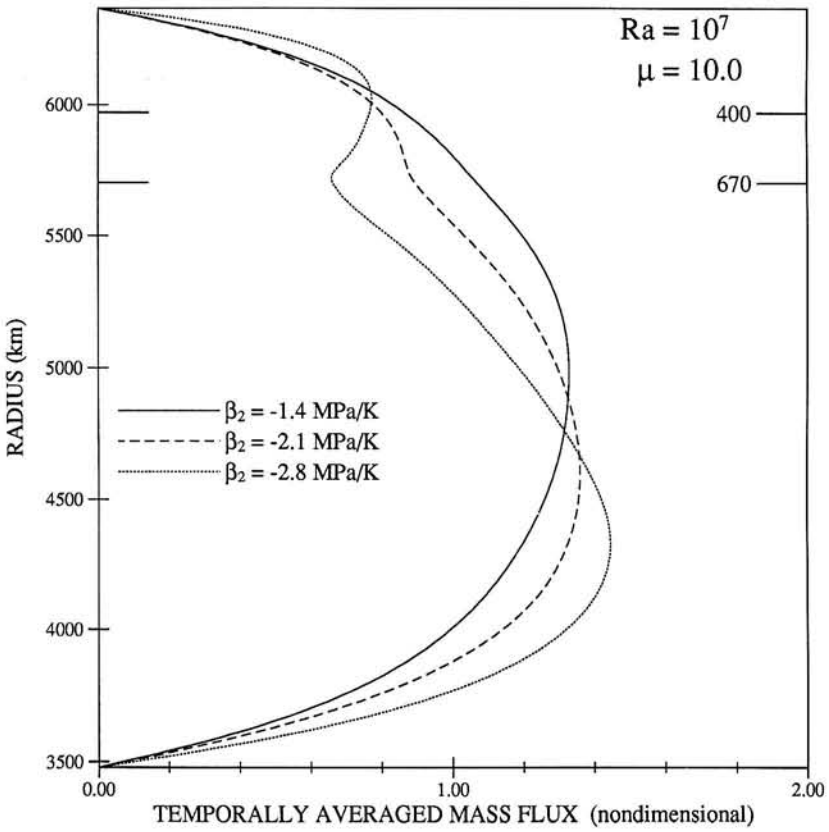

Figure 10. Temporally averaged mass flux functions (F_m) for three simulations in which the Rayleigh number is 10^7 and there is internal heating corresponding to $\mu = 10$. In all three simulations the Clapeyron slope of the 400-km phase boundary is +3 MPa/K and $h_1 = h_2 = 400$ (compare Figure 9). The three simulations differ only in the value of the 670-km Clapeyron slope. These values of β_2 are indicated.

400-km Clapeyron slope (+3.0 MPa/K versus +2.0 MPa/K) tends to decrease it, but this effect was found to be relatively small.

The mass flux data in Tables 3 and 4 have been plotted in Figure 11. Figure 11a shows the average absolute 400-km mass flux as a function of 670-km Clapeyron slope, while Figure 11b shows the 670-km mass flux versus β_2. The points with error bars drawn as solid lines come from the set of simulations in which $\mu = 0$, $\beta_1 = +2.0$ MPa/K, and $h_1 = h_2 = 50$, while the points with error bars drawn as dashed lines come from the set of simulations with $\mu = 10$, $\beta_1 = +3.0$ MPa/K, and $h_1 = h_2 = 400$. All four sets of points (i.e., 400-km and 670-km mass flux for both sets of simulations) have been fit to quadratic polynomials (of the form $a_0 + a_1\beta_2 + a_2\beta_2^2$), and these curves have been added to Figure 11 along with the values of the coefficients. Figure 11 clearly indicates the increased dependence on β_2 of the degree of layering in the latter set of simulations discussed above. Figure 11 indicates that it can be misleading to think that the degree of layering depends solely on the value of the 670-km Clapeyron slope. It is important therefore to keep this in mind when considering works in which only the Clapeyron slope is varied, such as those by *Christensen and Yuen* [1985] or *Machetel and Weber* [1991].

There are significant differences between the three geotherms of Figure 9. These three geotherms differ in a very obvious way, their shape, throughout the transition zone between 400 km and 670 km. In the layered flow (dotted line) there is clearly a thermal boundary layer with a negative gradient across it, as is characteristic of such flows. In the other two geotherms, however, the average temperature is raised a few degrees (≈90 K) at 400 km and lowered a few degrees (≈60 K) at 670 km. This raising and lowering of the average shell temperature at 400 km and 670 km, respectively, is a result of the release of latent heat into the mantle at the exothermic 400-km phase transition and the absorption of heat at the endothermic 670-km phase transition. In the simulation represented by the solid line, there is no layering at all. In fact, the mass flux at 670 km is larger than it would be if there were no phase boundaries present (see

Table 4. Values of the Layering Parameter P_{10} for the Three Simulations of Figure 9 and 10

	Mass Flux, km m^{-2} yr^{-1}		
β_2, MPa/K	400 km	670 km	P_{10}
−1.4	42.1	55.0	−0.13
−2.1	36.9	41.9	0.14
−2.8	22.1	21.2	0.56

The dimensional values of the 400-km and 670-km average absolute mass flux are included; $\mu = 10$; $\beta_1 = +3.0$ MPa/K; 25-km phase loops.

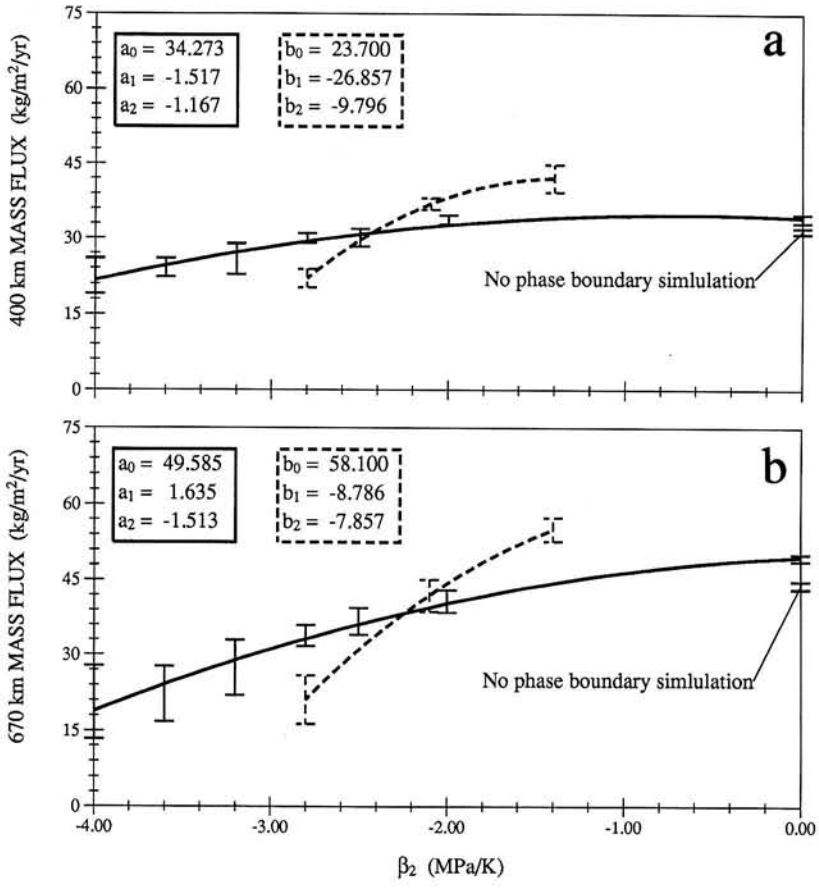

Figure 11. Temporally averaged values of the (a) 400-km and (b) 670-km mass flux as a function of the Clapeyron slope at 670 km. All the points shown are determined from simulations in which the Rayleigh number is 10^7. The two points not on any curve are values from a simulation in which no phase boundaries are present and there is no internal heating. These two points are indicated separately. The data points with error bars drawn as solid lines and fit by quadratic polynomials drawn as solid lines come from simulations in which there is no internal heating, the value of the 400-km Clapeyron slope is +2 MPa/K and $h_1 = h_2 = 50$. The data points with error bars drawn as dashed lines and fit by quadratic polynomials drawn as dashed lines come from simulations in which there is internal heating corresponding to $\mu = 10$, the value of the 400-km Clapeyron slope is +3 MPa/K and $h_1 = h_2 = 400$. The values of the coefficients of the quadratic fits are shown, outlined by their respective line types.

Table 4). Without the reduced mass flux that results in an internal thermal boundary layer at 670 km the effect of latent heat release on the geotherm becomes very evident.

On the Mechanism Responsible for Episodic Layering

In this final section we describe the physical mechanism responsible for the observed quasi-periodic nature of simulations in which the parameters are set so as to cause the flow to become layered. The nature of this time dependence has been described above. A simulation in which $Ra = 10^7$, $\mu = 0$, $\beta_1 = +3.0$ MPa/K, $\beta_2 = -2.8$ MPa/K, and $h_1 = h_2 = 200$ was used in that discussion. We employ this same simulation as a basis for discussing the underlying cause of this behavior.

Figure 12 shows five time series derived from the simulation under discussion. Figure 12a shows the 670-km average absolute mass flux that was shown in Figure 3. The times of occurrence of the avalanche events are clearly visible. Figures 12b–12e show aspects of the internal thermal boundary layer that develops across the endothermic transition at 670 km depth. The shaded area in Figure 12b represents the radial extent of this boundary layer as a function of time. Note, in particular, how the boundary layer grows to maximum thickness at the same point in time at which the avalanche events occur. It then thins abruptly and begins to thicken once more. Figure 12e presents the actual width of this boundary layer (δ_{670}) as a function of time. Figure 12d is the time dependence of the temperature drop across this boundary layer (ΔT_{670}). Finally, in Figure 12c we have determined a boundary layer Rayleigh number (Ra_{670}) based on δ_{670} and ΔT_{670} together with values of thermodynamic parameters at 670 km determined from the anelastic reference state functions. This Rayleigh number is defined as

$$Ra_{670} = \frac{g_{670}\alpha_{670}\Delta T_{670}\delta_{670}^3}{\kappa_{670}\nu_{670}}$$

It is the time dependence of this internal Rayleigh number that is of interest. Figure 12 clearly shows that Ra_{670} increases gradually and reaches its maximum just prior to the occurrence of an avalanche event, then decreases abruptly, and begins to grow slowly once more. There

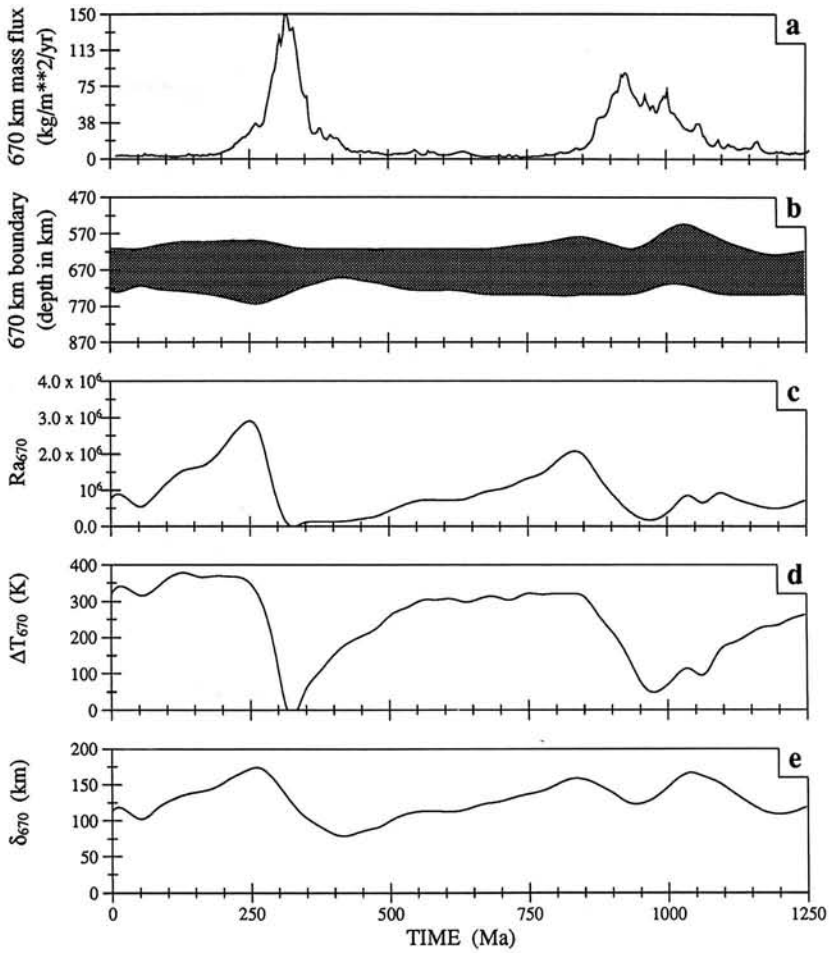

Figure 12. Time series showing the quasi-periodic behavior of the internal thermal boundary layer that develops at 670 km in flows that reside in the layered regime. These time series are from a simulation with a Rayleigh number of 10^7, no internal heating, $\beta_1 = +3.0$ MPa/K, $\beta_2 = -2.8$ MPa/K, and $h_1 = h_2 = 200$. This is the simulation used in text to portray the nature of time dependence in a layered flow. See the text for a complete description of Figures 12a–12e.

clearly appears to exist a threshold in Rayleigh number below which the boundary layer is stable. As the Rayleigh number passes this threshold, which on the basis of the data in Figure 12c has a value near 10^6, the boundary layer suddenly become unstable and an avalanche event occurs. The large radial mass flux characteristic of the avalanche reduces the local Rayleigh number until it falls below the critical value at which time the boundary layer becomes stable once more and the avalanche ceases. The temperature drop across the boundary begins to increase once more as the radial mass flux is inhibited by the phase transition. As the boundary layer broadens, Ra_{670} grows until it reaches its critical value again, and the cycle repeats. This scenario explains Figure 12 quite nicely. We see that Ra_{670} grows slowly, then suddenly decreases at the time of the avalanche event. ΔT_{670} undergoes a similar evolution, as does the boundary layer thickness δ_{670}. The observed temporal behavior of the layered solutions can therefore be explained as a growing and decaying internal boundary layer instability. This instability occurs when the boundary layer Rayleigh number exceeds its critical value.

The onset of this instability is localized in space and time at the points where the avalanches occur (see Plate 1). Ra_{670} of Figure 12 was determined based on instantaneous geotherms taken from the numerical simulation and thus is not a truly local Rayleigh number but rather a spatially averaged value at a particular instant of time. Because of this fact, Figure 12 is not appropriate for determining the precise value of the critical Rayleigh number. Moreover, a precise definition of where the extremities of the boundary layer are is required to determine any such critical value. This parameter does provide the basis for a clear qualitative explanation of the process, however, since the local Rayleigh number at any point remote from an avalanche will remain unchanged (or change very little) throughout the avalanche event, and so the variation in the local Rayleigh number at the actual avalanche site will dominate the time series.

Conclusions

We have developed a multiphase, anelastic, axisymmetric, mantle convection model which incorporates an Earth-like basic state. Numerical solutions of the governing system of equations were constructed for a number of parameter configurations, and these solutions were employed to isolate the influence of these parameters on the flow. In this analysis

we focused our attention on the impact upon the propensity for layering of each of the control variables. It was determined that either increasing Ra or μ or decreasing β_2 or the phase loop thickness had the effect of increasing the degree of layering in the flow. Increasing the value of β_1 tends to decrease the degree of layering. All of these results are valid for (at least) the parameter range $+2.0$ MPa/K $\leq \beta_1 \leq +3.0$ MPa/K, -4.0 MPa/K $\leq \beta_2 \leq 0.0$ MPa/K, $Ra = 10^7$, $50 \leq h_{1,2} \leq 400$ (200-km to 25-km phase loop thickness), and $0 \leq \mu \leq 10$. This is the parameter range in which Earth lives (except for phase loop thickness which is less than 25 km) and so is of particular interest. Whether Earth should be operating in a highly layered or partially layered state may only be determined once the parameter values are known more precisely (in particular, the value of β_2), but it seems safe to conjecture that the mantle is at least partially layered.

When the flow is in a partially layered state, an interesting quasi-periodic behavior is observed in the time dependence. The flow goes through periods of low mass flux across 670 km broken by shorter periods of high mass flux (a fact previously noted in the cursory analyses of both *Machetel and Weber* [1991] and *Peltier and Solheim* [1992] but not previously explained). During the high mass flux at 670-km events, localized "avalanches" of fluid are observed to penetrate the boundary. These avalanches appear suddenly and tend to cease just as abruptly. This intermittency in the degree of radial layering can be explained in terms of a growing and decaying instability that occurs in the internal thermal boundary layer which develops across the endothermic phase transition at 670 km depth in flows that exhibit partial layering. This growth and decay are driven by the difference in efficiency between the predominantly advective radial heat transport outside the 670-km thermal boundary layer and predominantly conductive radial heat transport within the thermal boundary layer. This difference causes a growth of the internal thermal boundary layer. When the temperature difference across the boundary layer and the boundary layer thickness become large enough to raise the local Rayleigh number above its critical value, an avalanche occurs in which fluid from the transition zone abruptly descends into the lower mantle, thus reducing the temperature gradient within the boundary layer and decreasing the local Rayleigh number below its critical value once more.

References

Akaogi, M., E. Ito, and A. Navrotsky, Olivine–modified spinel–spinel transitions in the system Mg_2SiO_4-Fe_2SiO_4: Calorimetric measurements, thermochemical calculation, and geophysical application, *J. Geophys. Res.*, *94*, 15,671–15,685, 1989.

Akimoto, S., and H. Fujisawa, Olivine-spinel transitions in the system Mg_2SiO_4-Fe_2SiO_4 at 800°C, *Earth Planet. Sci. Lett.*, *1*, 237–240, 1966.

Akimoto, S., Y. Matsui, and Y. Syono, High pressure crystal chemistry of orthosilicates and formation of the mantle transition zone, in *The Physics and Chemistry of Minerals and Rocks*, edited by R. G. J. Strens, pp. 327–365, John Wiley, New York, 1976.

Anderson, O. L., A. Chopelas, and R. Boehler, Thermal expansion vs. pressure at constant temperature: A re-examination, *Geophys. Res. Lett.*, *17*, 685–688, 1990.

Baumgardner, J. R., Three-dimensional treatment of convective flow in the Earth's mantle, *J. Stat. Phys.*, *39*, 501–511, 1985.

Bercovici, D., G. Schubert, and G. A. Glatzmaier, Three-dimensional spherical models of convection in the Earth's mantle, *Science*, *244*, 950–955, 1989.

Brown, J. M., and R. G. McQueen, Phase transitions, Gruneisen parameter, and elasticity for shocked iron between 77 GPa and 400 GPa, *J. Geophys. Res.*, *91*, 7485–7494, 1986.

Busse, F., and G. Schubert, Convection in fluid with two phases, *J. Fluid Mech.*, *46*, 801–812, 1971.

Christensen, U. R., and D. A. Yuen, Layered convection induced by phase transitions, *J. Geophys. Res.*, *90*, 10,291–10,300, 1985.

Davies, G. F., Thermal histories of convective earth models and constraints on radiogenetic heat production in the earth, *J. Geophys. Res.*, *85*, 2517–2530, 1980.

Dziewonski, A. M., and D. L. Anderson, Preliminary reference Earth model, *Phys. Earth Planet. Inter.*, *25*, 297–356, 1981.

Glatzmaier, G. A., Numerical simulations of mantle convection: Time-dependent, three-dimensional, compressible, spherical shell, *Geophys. Astrophys. Fluid Dyn.*, *43*, 223–264, 1988.

Glatzmaier, G. A., G. Schubert, and D. Bercovici, Chaotic, subduction-like downflows in a spherical model of convection in the Earth's mantle, *Nature*, *347*, 274–277, 1990.

Hsui, A. T., D. L. Turcotte, and K. E. Torrance, Finite-amplitude thermal convection within a self-gravitating fluid sphere, *Geophys. Fluid Dyn.*, *3*, 35–44, 1972.

Ito, E., The absence of oxide mixture in high-pressure phases of Mg-silicates, *Geophys. Res. Lett.*, *4*, 72–74, 1977.

Ito, E., and E. Takahashi, Postspinel transformations in the system Mg_2SiO_4-Fe_2SiO_4 and some geophysical implications, *J. Geophys. Res.*, *94*, 10,637–10,646, 1989.

Ito, E., M. Akaogi, L. Topor, and A. Navrotsky, Negative pressure-temperature slopes for reactions forming $MgSiO_3$ perovskite from calorimetry, *Science*, *249*, 1275–1278, 1990.

Jarvis, G. T., and D. P. McKenzie, Convection in a compressible fluid with infinite prandtl number, *J. Fluid Mech.*, *96*, 515–583, 1980.

Jeanloz, R., and D. L. Heinz, Experiments at high temperature and pressure: Laser heating through the diamond cell, *J. Phys. C Solid State Phys.*, *45*(C8), 83–92, 1984.

Jeanloz, R., and S. Morris, Temperature distribution in the crust and mantle, *Annu. Rev. Earth Planet. Sci.*, *14*, 377–415, 1986.

Jeanloz, R., and A. B. Thompson, Phase transitions and mantle discontinuities, *Rev. Geophys.*, *21*, 51–74, 1983.

Katsura, T., and E. Ito, The system Mg_2SiO_4-Fe_2SiO_4 at high pressures and temperatures: precise determination of stabilities of olivine, modified spinel, and spinel, *J. Geophys. Res.*, *94*, 15,663–15,670, 1989.

Kieffer, S. W., Lattice thermal conductivity within the earth and considerations of a relationship between the pressure dependence of thermal diffusivity and the volume dependence of the Gruneisen parameter, *J. Geophys. Res.*, *81*, 3025–3029, 1976.

Liu, L. G., Post-oxide phases of forsterite and enstatite, *Geophys. Res. Lett.*, *2*, 417–419, 1975.

Liu, L. G., The post-spinel phases of forsterite, *Nature*, *262*, 770–772, 1976.

Machetel, P., and M. Rabinowicz, Three-dimensional convection in spherical shells, *Geophys. Astrophys. Fluid Dyn.*, *37*, 57–84, 1986.

Machetel, P., and P. Weber, Intermittent layered convection in a model mantle with an endothermic phase change at 670 km, *Nature*, *350*, 55–57, 1991.

Machetel, P., and D. A. Yuen, Penetrative convective flows induced by internal heating and mantle compressibility, *J. Geophys. Res.*, *94*, 10,609–10,626, 1989.

Moré, J., B. Garbow, and K. Hillstrom, User guide for MINPACK-1, *Tech. Rep. ANL-80-74*, Argonne Natl. Lab., Argonne, Ill., 1980.

Müller, D. E., A method for solving algebraic equations using an automatic computer, *Math. Tables Aids Comput.*, *10*, 208–215, 1956.

Osako, M., and E. Ito, Thermal diffusivity of $MgSiO_3$ perovskite, *Geophys. Res. Lett.*, *18*, 239–242, 1991.

Peltier, W. R., Penetrative convection in the planetary mantle, *Geophys. Fluid Dyn.*, *5*, 47–88, 1972.

Peltier, W. R., Mantle convection and viscoelasticity, *Annu. Rev. Fluid Mech.*, *17*, 561–608, 1985.

Peltier, W. R., and G. T. Jarvis, Whole mantle convection and the thermal evolution of the Earth, *Phys. Earth Planet. Inter.*, *29*, 281–304, 1982.

Peltier, W. R., and L. P. Solheim, Mantle phase transitions and

layered chaotic convection, *Geophys. Res. Lett.*, *19*, 321–324, 1992.

Peltier, W. R., J. T. Jarvis, A. M. Forte, and L. P. Solheim, The radial structure of the mantle general circulation, in *Mantle Convection: Plate Tectonics and Global Dynamics*, edited by W. R. Peltier, pp. 765–815, Gordon and Breach, New York, 1989.

Reynard, B., and G. D. Price, Thermal expansion of mantle minerals at high pressures—A theoretical study, *Geophys. Res. Lett.*, *17*, 689–692, 1990.

Richter, F. M., Finite amplitude convection through a phase boundary, *Geophys. J. R. Astron. Soc.*, *35*, 265–276, 1973.

Ringwood, A. E., *Composition and Petrology of the Earth's Mantle*, McGraw-Hill, New York, 1975.

Ringwood, A. E., and A. Major, Synthesis of Mg_2SiO_4-Fe_2SiO_4 spinel solid solutions, *Earth Planet. Sci. Lett.*, *1*, 241–245, 1966.

Ringwood, A. E., and A. Major, The system Mg_2SiO_4-Fe_2SiO_4 at high pressures and temperatures, *Phys. Earth Planet. Inter.*, *3*, 89–108, 1970.

Schubert, G., and A. Zebib, Thermal convection of an internally heated infinite prandtl number fluid in a spherical shell, *Geophys. Astrophys. Fluid Dyn.*, *15*, 65–90, 1980.

Schubert, G., D. A. Yuen, and D. L. Turcotte, Role of phase transitions in a dynamic mantle, *Geophys. J. R. Astron. Soc.*, *42*, 705–735, 1975.

Sharpe, H. N., and W. R. Peltier, Parameterized mantle convection and the Earth's thermal history, *Geophys. Res. Lett.*, *5*, 737–740, 1978.

Sharpe, H. N., and W. R. Peltier, A thermal history model for the Earth with parameterized convection, *Geophys. J. R. Astron. Soc.*, *59*, 171–203, 1979.

Shearer, P. M., Seismic imaging of upper-mantle structure with new evidence for a 520-km discontinuity, *Nature*, *344*, 121–126, 1990.

Solheim, L. P., and W. R. Peltier, Heat transfer and the onset of chaos in a spherical, axisymmetric, anelastic model of whole mantle convection, *Geophys. Astrophys. Fluid Dyn.*, *53*, 205–255, 1990.

Solheim, L. P., and W. R. Peltier, Mantle phase transitions and layered convection, *Can. J. Earth Sci.*, in press, 1993.

Stacey, F. D., A thermal model of the Earth, *Phys. Earth Planet. Inter.*, *15*, 341–348, 1977.

Tackley, P. J., D. J. Stevenson, G. A. Glatzmaier, and G. Schubert, Effects of an endothermic phase transition at 670 km depth on spherical mantle convection, *Nature*, *361*, 699–704, 1993.

Turcotte, D. L., On the thermal evolution of the Earth, *Earth Planet. Sci. Lett.*, *48*, 53–58, 1980.

Weidner, D. J., A mineral physics test of a pyrolite mantle, *Geophys. Res. Lett.*, *12*, 417–420, 1985.

Weidner, D. J., H. Sawamoto, S. Sasaki, and M. Kumazawa, Single-crystal elastic properties of the spinel phase of Mg_2SiO_4, *J. Geophys. Res.*, *89*, 7852–7860, 1984.

Weir, A. D., Axisymmetric convection in a rotating sphere, 1, Stress-free surface, *J. Fluid Mech.*, *75*, 49–79, 1976.

Weir, A. D., Axisymmetric convection in a rotating sphere, 2, Non-slip surface, *Geophys. Astrophys. Fluid Dyn.*, *11*, 205–222, 1978.

Young, R. E., Finite-amplitude thermal convection in a spherical shell, *J. Fluid Mech.*, *63*, 695–721, 1974.

Zebib, A., G. Schubert, and J. M. Straus, Infinite prandtl number thermal convection in a spherical shell, *J. Fluid Mech.*, *97*, 257–277, 1980.

Zebib, A., G. Schubert, J. L. Dein, and R. C. Paliwal, Character and stability of axisymmetric thermal convection in spheres and spherical shells, *Geophys. Astrophys. Fluid Dyn.*, *23*, 1–42, 1983.

Zebib, A., A. K. Goyal, and G. Schubert, Convective motions in a spherical shell, *J. Fluid Mech.*, *152*, 39–48, 1985.

W. R. Peltier and L. P. Solheim, Department of Physics, University of Toronto, Toronto, Ontario, Canada M5S 1A7.

(Received November 18, 1992; revised July 22, 1993; accepted July 27, 1993.)